The odd-number cyclo[13]carbon and its dimer cyclo[26]carbon

Authors: Florian Albrecht,[1†] Igor Rončević,[2†] Yueze Gao[2†], Fabian Paschke[1†], Alberto Baiardi[3], Ivano Tavernelli[3], Shantanu Mishra[1], Harry L. Anderson[2]* and Leo Gross[1]*

Affiliations:

[1] IBM Research Europe – Zürich, 8803 Rüschlikon, Switzerland.

[2] Department of Chemistry, Oxford University, Chemistry Research Laboratory, Oxford, United Kingdom.

[3] IBM Quantum, IBM Research Europe – Zürich, 8803 Rüschlikon, Switzerland.

† These authors contributed equally.

*Corresponding authors. Email: harry.anderson@chem.ox.ac.uk; lgr@zurich.ibm.com

Abstract: Molecular rings of *N* carbon atoms (cyclo[*N*]carbons, or C_N) are excellent benchmarking systems for testing quantum chemical theoretical methods, and valuable precursors to other carbon-rich materials. Odd-*N* cyclocarbons, which have been elusive to date, are predicted to be even less stable than even-*N* ones. We report the on-surface synthesis of cyclo[13]carbon, C_{13}, by manipulation of decachlorofluorene with a scanning probe microscope tip. We elucidate the properties of C_{13} by experiment and theoretical modelling. C_{13} adopts an open-shell configuration with a triplet ground state and a kinked geometry, which shows different extents of distortion and carbene localization, depending on the molecular environment. Moreover, we prepare and characterize the C_{13} dimer, cyclo[26]carbon, demonstrating the potential of cyclocarbons and their precursors as building blocks for carbon allotropes.

One-Sentence Summary: Cyclo[13]carbon has an open-shell ground state, a carbene center and dimerization of its precursors yields cyclo[26]carbon.

Main Text: Recently, the family of carbon allotropes was expanded by the generation and on-surface characterization of cyclo[*N*]carbons (C_N), molecular rings composed of *N* carbon atoms. Several even-*N* cyclocarbons have been structurally characterized (*1-4*). Cyclocarbons are relatively small, and their electronic structure resembles that of a particle on a ring and can be rationalized with text-book physics (*5-7*). However, the many energy-degenerate orbitals and the possibility of multiple Jahn-Teller distortions render calculations extremely demanding (*7-14*), making cyclocarbons excellent model systems for benchmarking theoretical approaches (*15*). Moreover, their monocyclic structures make them interesting systems in the context of aromaticity (*1-4, 11-14*). For many years, experimental investigations of cyclocarbons were limited to studies in the gas phase (*16, 17*) or in a solid matrix (*18*). Only recently, even-*N* cyclocarbons with N = 10, 12, 14, 16, 18, 20 (*1-4*) have been generated by on-surface synthesis (*19*) using atom manipulation techniques and were characterized by non-contact atomic force microscopy (AFM) with CO functionalized tips (*20*) and scanning tunnelling microscopy (STM) on NaCl surfaces at low temperature.

Even-*N* cyclocarbons can be doubly aromatic, with $N = (4k + 2)$, where k is an integer, or doubly anti-aromatic with $N = 4k$. In agreement with recent theoretical predictions (*12*), the doubly aromatic ($4k + 2$) cyclocarbons show substantial bond-angle alternation (BAA) and no measurable bond-length alternation (BLA) for $N < 14$ (*3*), but large BLA for $N > 14$ (*1, 21*) (as well as for C_{26}, characterized below in this work). In this series, C_{14} is the transition structure, with small BLA and strong BAA (*3, 12*). All the $4k$ cyclocarbons studied show strong BLA indicative of a doubly anti-aromatic ground state (*2, 4*).

In general, even-*N* cyclocarbons exhibit $N/2$ symmetry, that is, $C_{(N/2)h}$ or $D_{(N/2)h}$, a closed-shell singlet ground state, and the structural distortions to be considered are only BLA and BAA. In contrast, odd-*N* cyclocarbons cannot form $C_{(N/2)h}$ nor $D_{(N/2)h}$ geometries but might adopt more symmetric shapes such as D_{Nh} or more distorted shapes such as C_s or C_{2v}, and are expected to be even less stable than even-*N* cyclocarbons (*10, 11*). In addition, an odd number of electrons in the π-systems increases the number of ground states that need to be considered, including open-shell and high-spin configurations (*13*). Moreover, localized carbene centers can occur as an additional element of distortion. Odd-*N* cyclocarbons have similarities to cycloalkenylidene carbenes C_nH_{n-1} in which different carbene centers and spin ground states have been discussed (*22-26*), but in the latter, the carbene center is fixed at the only hydrogen-free carbon atom, whereas in odd-*N* cyclocarbons the carbene center could be delocalized over several carbon atoms by resonance. Thus odd-*N* cyclocarbons are structurally highly complex and extremely challenging to predict (*8, 11, 13*).

Here, we report the experimental structural characterization of the odd-*N* cyclocarbon C_{13}, in conjunction with theoretical modeling. Inspired by precursors used by Sun *et al.* (*3*), we prepared C_{13}, a cyclocarbon of the $N = (4k + 1)$ series, on ultrathin NaCl films on Au(111) by tip-induced dehalogenation of decachlorofluorene ($C_{13}Cl_{10}$). We used AFM and STM to gain insight into the geometry and electronic structure. We observed some C_{13} molecules with a pronounced kink, indicating a localized angular carbene center. At other adsorption sites, the kink was less pronounced, which resulted in a rounder shape and indicated that the extent of carbene localization depends on the local environment. Our results show that C_{13} has an open-shell ground state with 13 electrons in both its π-systems, with a triplet indicated by theory. Taking advantage of the high reactivity of odd-number cyclocarbons, the larger cyclo[26]carbon (C_{26}) was formed through dehalogenation and dimerization of two $C_{13}Cl_{10}$ precursors. Orbital density

maps of C_{26} visualize pairs of its energy degenerate molecular frontier orbitals, experimentally revealing its electronic structure.

On-surface synthesis of C_{13}

The precursor decachlorofluorene, $C_{13}Cl_{10}$ (Fig. 1A top panel; for synthesis see figs. S1 to S3) was sublimed by fast heating from a Si wafer onto an Au(111) surface partially covered with monolayer (ML, one-atom thick) and bilayer (BL, two-atoms thick) NaCl films at a sample temperature of about T = 10 K. For an overview STM image see fig. S4. Characterization by STM and AFM in noncontact mode was performed with CO tip functionalization (*20*) at T = 5 K, typically on ML NaCl.

AFM images were obtained in constant-height mode, with the tip-height offset Δz added to the tip-sample distance of the STM-controlled set point. AFM-far images are recorded at the onset of atomic resolution, that is, the largest Δz that yielded atomic resolution. For AFM-close images, Δz was reduced by about 0.3 Å with respect to AFM-far. At AFM-far, bond-order related contrast is typically observed as brightness contrast in the Δf-map (the larger the bond order, the brighter the appearance), explained by Pauli repulsion (*27*). At AFM-close, bond-order differences result in different apparent bond length (the larger the bond order, the shorter the apparent bond length), because of CO-tip relaxations (*27*, *28*). CO-tip relaxations also lead to an apparent sharpening of bonds and distortions (apparent expansion) of structures, at their peripheries (*27*, *28*). This is the reason for the larger, distorted appearance of the partially dechlorinated rings, for example in Fig. 1D and E (see fig. S5).

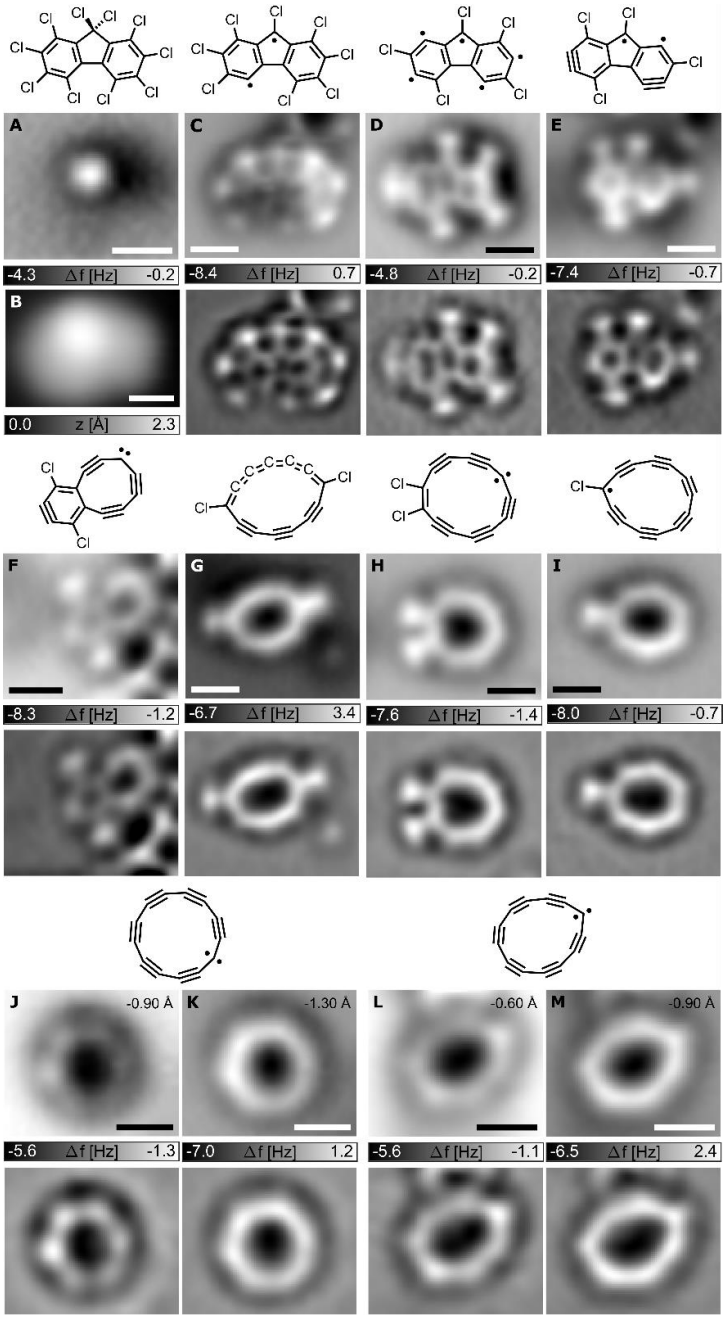

Fig. 1. On-surface synthesis of C_{13}. (**A**) Precursor, AFM data with a tip-height offset Δz = 0.7 Å from the setpoint of V = 0.2 V and I = 0.5 pA, and (**B**) STM data, V = 0.2 V, I = 0.5 pA. (**C** to **I**) Intermediates observed after applying voltage pulses on precursors. AFM raw data in upper panels and Laplace-filtered data in the respective lower panels. Tentatively assigned Kekulé structures are shown above each panel. (**J** to **M**) Two individual C_{13} molecules, with different structural distortion, that is, "round" (J and K) and "kinked" (L and M), at AFM-far (J and L) and AFM-close (K and M) with tip-height offsets Δz indicated. All scale bars 5 Å.

We found intact precursor molecules as shown in Fig. 1A and B. Because of its nonplanarity, we only observed one bright feature in AFM (Fig. 1A), at the position of a protruding Cl atom bonded to the sp^3 hybridized C atom of the central CCl_2 unit. Voltage pulses of up to V = 4.5 V

with currents *I* on the order of a few pA, applied for a few 100 ms, were used to unmask precursor molecules by dehalogenation on ML NaCl. Usually, such voltage pulses resulted in dissociation of several Cl atoms and Fig. 1, C to I show some of the observed intermediates, which indicated that retro-Bergman reactions (*29. 30*) were induced, see also figs. S5 to S9.

Successively applied voltage pulses led to formation of C_{13} (Fig. 1, J to M, and figs. S5 to S15). We generated 25 individual C_{13} molecules on the surface with a yield of about 40%, using the described voltage pulses. In unsuccessful attempts, the ring opened to form linear or branched polyynic chains (see fig. S10) or the molecule was picked up by the tip. Up to two Cl adatoms could be reversibly reattached (*31*) to C_{13}, resulting in structures such as shown in Fig. 1, G, H, and I (see also fig. S7). We observed C_{13} in a range of different shapes, varying from a "round" shape (see Fig. 1, J and K) to a more distorted, "kinked" geometry (see Fig. 1, L and M, and figs. S11 to S15). All results shown are measurements on ML NaCl. On BL NaCl, dehalogenated products could only be stably imaged in a few cases without moving them (see fig. S12), indicating a small diffusion barrier.

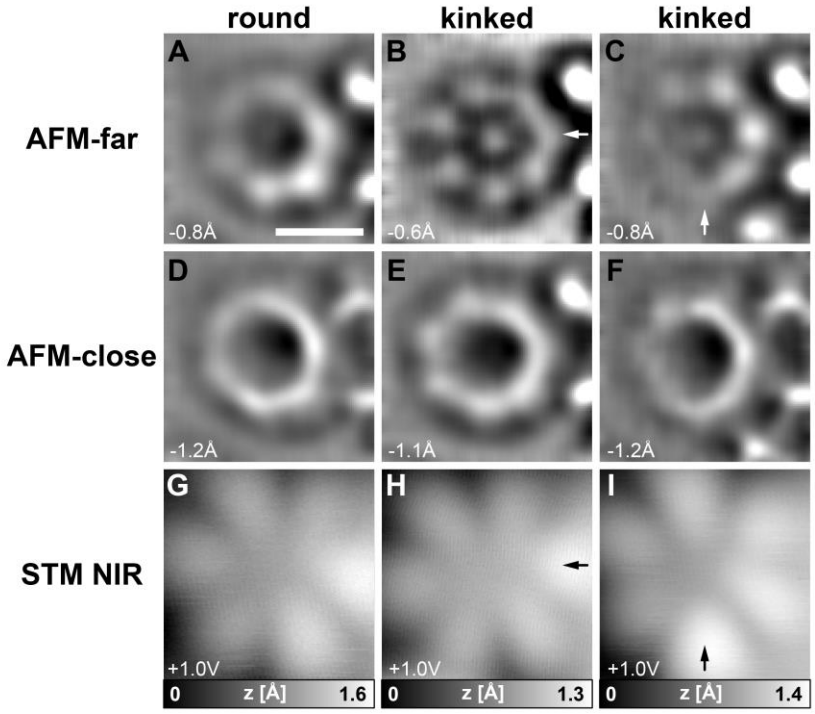

Fig. 2. Electronic characterization of C_{13}. (**A** to **C**) AFM-far, (**D** to **F**) AFM-close, Δ*z* indicated. Laplace-filtered data, for raw data, see fig. S14. (**G** to **I**) STM data, $V = 1.0$ V, $I = 0.5$ pA. All panels show the same individual molecule, adsorbed on ML NaCl at three different sites next to a BL NaCl step-edge, which is located on the right-hand side in all panels. For the "kinked" C_{13} (2nd and 3rd column), the location of the kink is indicated by arrows. Scale bar 5 Å, applies to all images.

The extent of distortion in individual C_{13} molecules was different at different adsorption sites (see Fig. 2 and figs. S11 to S15), indicating that the shape was influenced by the surface environment (*2*). "Round" C_{13} molecules exhibit six bright lobes in AFM-far (Fig. 1J), whereas

in AFM-close, they show pronounced edges on one side of the ring and a rounder shape on the opposing side (Fig. 1K). The more distorted, "kinked" C_{13} molecules exhibited seven lobes in AFM-far (Fig. 1L), whereas at AFM-close, they exhibited the shape of a squeezed heptagon (Fig. 1M).

Figure 2 shows AFM and STM data of the same individual C_{13} molecule at different adsorption sites next to a BL NaCl island. In Fig. 2A, the molecule exhibited "round" and in Fig. 2, B and C, "kinked" shapes. We observed that the extent of kinking varied smoothly across different environments, rather than defining two discrete geometries (see also fig. S15). At the BL NaCl step-edge, the molecule was adsorbed with sufficient stability to obtain STM maps at the negative ion resonance (NIR), that is, transiently attaching an electron into a low-energy unoccupied molecular orbital (*32*), as shown in Fig. 2, G to I. For all observed shapes, the STM maps showed six lobes of high orbital density. For the "kinked" C_{13} we observed signatures of in-plane orbital densities at slightly lower *V* than for out-of-plane orbitals (fig. S12 and Fig. 3L).

Theory results on C_{13}

Cyclocarbons exhibit two orthogonal π-systems, one "in-plane" with orbital lobes in the plane of the nuclei (shown in orange in Fig. 3A), and one "out-of-plane" with zero density in the molecular plane (blue in Fig. 3A). According to a double particle-on-a-ring model, C_{13} has four π-orbitals, near the Fermi energy, two of the in-plane π-system and two of the out-of-plane π-system, as shown in Fig. 3A (*9, 14*). Neutral C_{13} has six electrons in these four frontier orbitals and different occupation of these orbitals results in several possible electronic states. Without assuming which is the ground state, we can label these states according to the occupation of their frontier in-plane orbitals (first two numbers) and out-of-plane orbitals (second two numbers).

In an infinitely large ring with no BAA, the two π-systems are degenerate. However, inducing stress due to a finite ring size lifts the energy degeneracy of in-plane and out-of-plane systems. The out-of-plane orbital energies become slightly lower than their in-plane counterparts (*9, 14*). Therefore, in the absence of both BLA and BAA (D_{13h} geometry), the in-plane orbitals *A′* and *B′* would be singly occupied, whereas their out-of-plane counterparts *A″* and *B″* would be doubly occupied, resulting in a triplet ground state $^3|11\ 22\rangle$, see Fig. 3B.

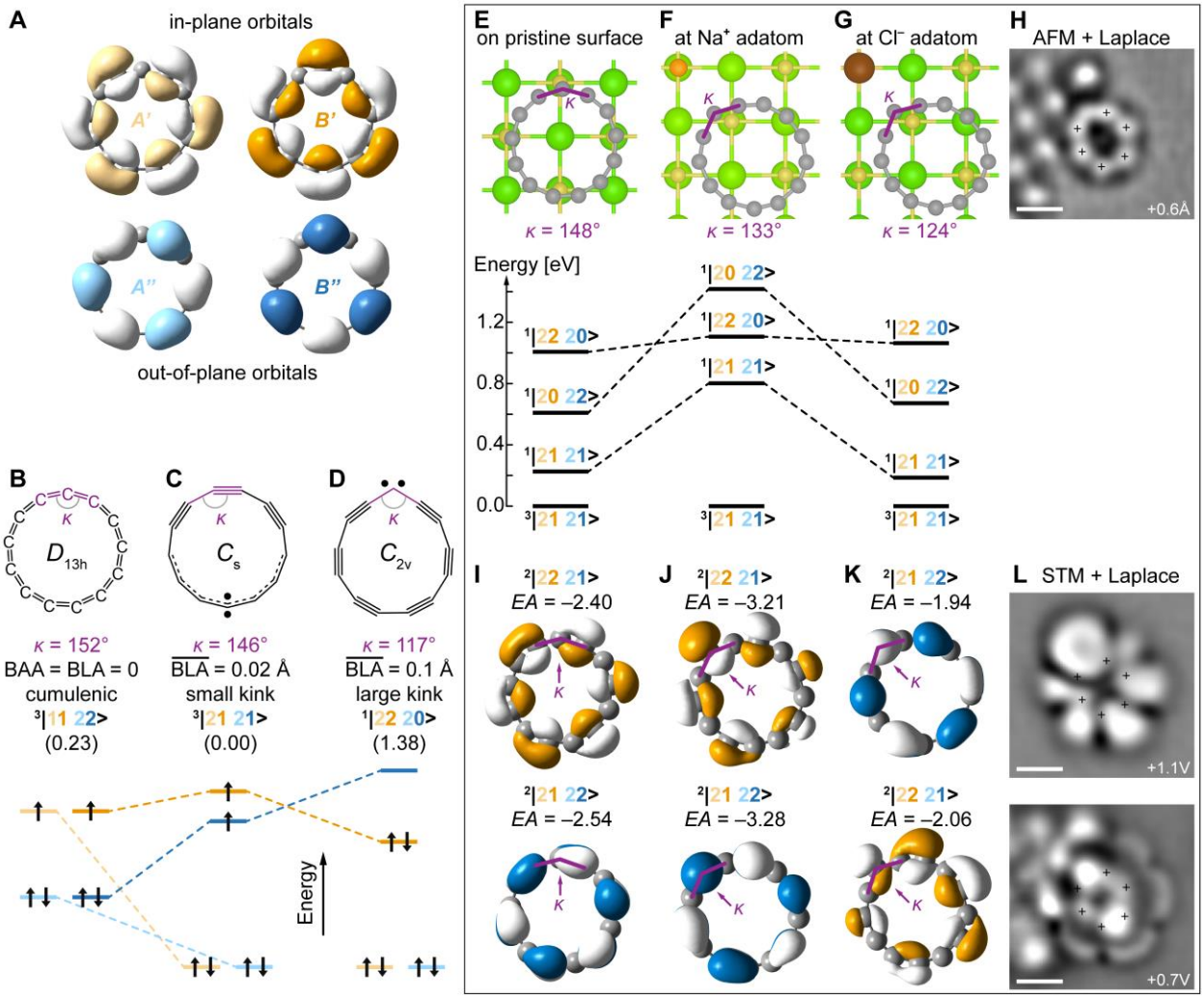

Fig. 3. **Theoretical investigation of C_{13}.** (**A**), Frontier orbitals of C_{13} in D_{13h} geometry. (**B** to **D**), CASPT2 optimized geometries and relative energies (in eV) of C_{13} in the gas phase, with averaged BLA indicated. (**B**) A D_{13h} cumulenic structure. (**C**) The $^3|21\ 21\rangle$ triplet state, which is found to be the ground state. (**D**) The $^1|22\ 20\rangle$ closed-shell singlet state. (**E** to **G**) On-surface calculations for C_{13}, (**E**) on a pristine NaCl surface, (**F**) Next to a positively charged adatom, and (**G**) next to a negatively charged adatom. Energies of several singlet states, relative to the $^3|21\ 21\rangle$ triplet ground state in the respective geometry, are indicated. (**H**) AFM image of "kinked" C_{13}. (**I** to **K**) Dyson orbitals for the transitions to the two lowest anionic charge states from the $^3|21\ 21\rangle$ state in the geometries of (E to G) respectively, with electron affinity (*EA*) in eV indicated. (**L**) Laplace-filtered STM images of "kinked" C_{13} at indicated *V*, corresponding to out-of-plane (top) and in-plane (bottom) orbitals. For more theory results, see figs. S16 to S21, for details on (H and L), see fig. S12.

Introducing BLA lowers the energy of *A* orbitals and increases the energy of their *B* counterparts. This effect results in the triplet $^3|21\ 21\rangle$ ground state (see Fig. 3C), with 13 electrons in both π-systems, which adopts a shape with a small kink (the smallest bond angle is $\kappa = 146°$, smaller than $\kappa = 152°$ for the D_{13h} geometry) and an irregular pattern of BLA. A structure with a larger kink ($\kappa = 117°$) was found by optimizing the geometry of the $^1|22\ 20\rangle$ closed-shell singlet state

(see Fig. 3D). The $^3|21\ 21>$ and $^1|22\ 20>$ states were predicted to have similar energies by Baryshnikov *et al*. (*13*), with CASSCF (complete active space self-consistent field) and DFT (density functional theory) calculations. The $^3|21\ 21>$ open-shell structure with a small kink (Fig. 3C) can be considered a delocalized *sp* carbene. The $^1|22\ 20>$ closed-shell structure (Fig. 3D) can be described as a localized sp^2 carbene that contributes the lone electron pair in its sp^2 hybridized orbital to the in-plane π-system and an empty *p* orbital to the out-of-plane π-system (*13*).

Our CASPT2 (complete active space perturbation theory) calculations (details in Methods Section), which add dynamic correlation on top of a self-consistent CAS wavefunction, indicated that the triplet $^3|21\ 21>$ state is the global minimum of C_{13}, both in the gas phase (Fig. 3C) and for different adsorption environments on the NaCl surface (Fig. 3, E to G). Explicitly correlated coupled clusters calculations also predicted a triplet ground state (fig. S20). This is not surprising as the singly-occupied in-plane (*B′*) and out-of-plane (*B″*) orbitals are close in energy due to their similar nodal structure (Fig. 3A), and the lack of overlap between them results in ferromagnetic coupling (*33*).

In the gas phase (Fig. 3C) and on a pristine surface (Fig. 3E), the C_{13} at its triplet minimum exhibits a small kink (κ = 146° to 148°) and small BLA. The kink became more pronounced when the molecule interacted with surface defects, such as adatoms (Fig. 3, F and G) and the spin density became more localized at the kink (fig. S18), but the ground state remained $^3|21\ 21>$. In all considered geometries, the states with closed-shell configurations as major contributions were >0.6 eV above the triplet ground state (Fig. 3, E to G).

Electronic characterization of C_{13}

We compared the STM maps of the NIR (Fig. 2, G to I) with calculated Dyson orbitals for electron attachment $<\psi^{n+1}|\psi^n>$, where *n* is the number of electrons (*34*, *35*). Vertical attachment of an electron to C_{13} in the triplet ground state $\psi^n = {}^3|21\ 21>$ can result in an electronic state with doubly occupied out-of-plane orbitals $\psi^{n+1} = {}^2|21\ 22>$ or doubly occupied in-plane orbitals $\psi^{n+1} = {}^2|22\ 21>$. Interestingly, electron affinities (*EA*) for the in-plane and out-of-plane system for a certain geometry were similar (within ~0.15 eV), with more kinked geometries energetically favoring electron attachment to the in-plane π-system (see fig. S17). The computed *EA* values strongly depended on the electrostatics of the environment, ranging from about –3.3 eV for adsorption near a positive adatom (Fig. 3 J) to –2.5 eV on a pristine surface (Fig. 3 I) and –2.1 eV for adsorption near a negative adatom (Fig. 3 K).

The Dyson orbitals of both transitions are shown in Fig. 3, I to K (for the respective on-surface geometries see fig. S17 and for Dyson orbitals calculated using a quantum-computing algorithm see fig. S19). Because of the large (~0.3 eV) energy broadening of the ionic resonances on NaCl (*32*) and the larger extension of the out-of-plane orbitals towards the tip than the in-plane orbitals, we expected that the respective out-of-plane Dyson orbitals (drawn in blue) would dominate the STM contrast, and that the in-plane orbitals would be challenging to resolve in the experiment (see Fig. 3L and fig. S12). Although the geometric distortion did not change the nodal plane structure of the Dyson orbitals, it did affect the extent of delocalization (that is, the intensity of the lobes) and ordering of the $^2|21\ 22>$ and $^2|22\ 21>$ states. In the case of a more pronounced kink, the Dyson orbital usually became more localized at the kink (Fig. 3, I to K, and figs. S12, S17 and S19).

The "kinked" C_{13} was well described by adsorption next to a Cl^- adatom (Fig. 3K), as the NIR showed a more pronounced lobe above the kink (Fig. 2, H and I, Fig. 3 H and L, and fig. S12) and the in-plane orbital was observed closer to the Fermi energy than the out-of-plane orbital (see Fig. 3L and fig. S12). Note, that an in-plane density at the NIR (Fig. 3L bottom panel and fig. S12) would not be observed if the ground state was ^{1}|22 20>. The "round" C_{13} was well described by the C_{13} on the pristine surface (Fig. 3 E and I). Lobes of the NIR were between short bonds on the side of the molecule with strong BLA, that is, the side that showed more pronounced edges in AFM-close (Fig. 2D).

Discussion of C_{13}

Comparing experiment and theory, we conclude that the adsorbed C_{13} molecules were all in the |21 21> state with an *sp* carbene center. We excluded the ^{3}|11 22> state (Fig. 3B), because of the observed BLA in AFM data and the detection of out-of-plane orbital densities at the NIR. We excluded the ^{1}|22 20> state (Fig. 3D), because of the detection of an in-plane orbital at the NIR of the "kinked" C_{13} (Fig. 3L and fig. S12). Comparison of STM orbital densities obtained at the NIR to Dyson orbitals with ^{3}|21 21> as the initial state was excellent, reproducing changes in relative intensities and energies related to the extent of the kink in C_{13} (Fig. 3, I to L). By theory we find that the triplet ^{3}|21 21> state is lower in energy compared to the open-shell singlet ^{1}|21 21> state in all calculated geometries (Fig. 3 E to G and fig. S20).

C_{13} exhibited geometries with a differently pronounced kink, indicating various extents of structural distortion, related to different localization of the carbene center, depending on the surface environment. Although the carbene was delocalized over several carbon sites in the "round" C_{13}, it became more localized on a specific carbon in the "kinked" C_{13}. Thus, the "kinked" C_{13} relates to the cycloalkenylidene carbenes C_5H_4 and C_7H_6, which have a $\sigma^1\pi^1$ carbene center (*22*-*26*), where the σ and π symbols correspond to the singly occupied in-plane (*B′*) and out-of-plane (*B′′*) orbitals in "kinked" C_{13}, respectively.

Our DFT calculations (fig. S21) indicated that C_{13} in its ^{3}|21 21> ground state sustains an anti-aromatic ring current of about –18 nA/T ($NICS(2)_{zz}$ = +22.5 ppm), slightly weaker than the –25 nA/T current reported in the doubly (Hückel) anti-aromatic C_{16} (*12*, *14*), in which both π-systems produce an anti-aromatic current. The ^{3}|21 21> ground state of C_{13}, in contrast to the strongly anti-aromatic ^{1}|22 20> excited state (*13*,*14* see fig. S21), cannot be discussed in terms of Hückel nor Baird aromaticity rules, because of an odd number of electrons in both π-systems. We also note that the ring current in C_{13} is likely to be very sensitive to geometry, as it is composed of competing aromatic and anti-aromatic contributions, suggesting a possibility of aromaticity reversals (*14*).

Dimerization to form C_{26}

Applying voltage pulses above two neighboring C_{13} precursors on the surface yielded the molecule shown in Fig. 4 (see also figs. S22 to S24), which we assigned as C_{26}, a cyclo[*N*]carbon of the $N = (4k + 2)$ series. We hypothesize that C_{26} formed from two C_{13}, but it is also possible that dimerization occurred before complete dehalogenation. We did not resolve intermediates of C_{26} that would indicate the order of dehalogenations, dimerization, and ring openings. Partly dechlorinated dimers of decachlorofluorene could not be completely dechlorinated to yield C_{26} (see fig. S25). The AFM contrast of C_{26} (Fig. 4, A and B, see also fig. S23) indicated pronounced BLA, and thus a polyynic structure (Fig. 4C).

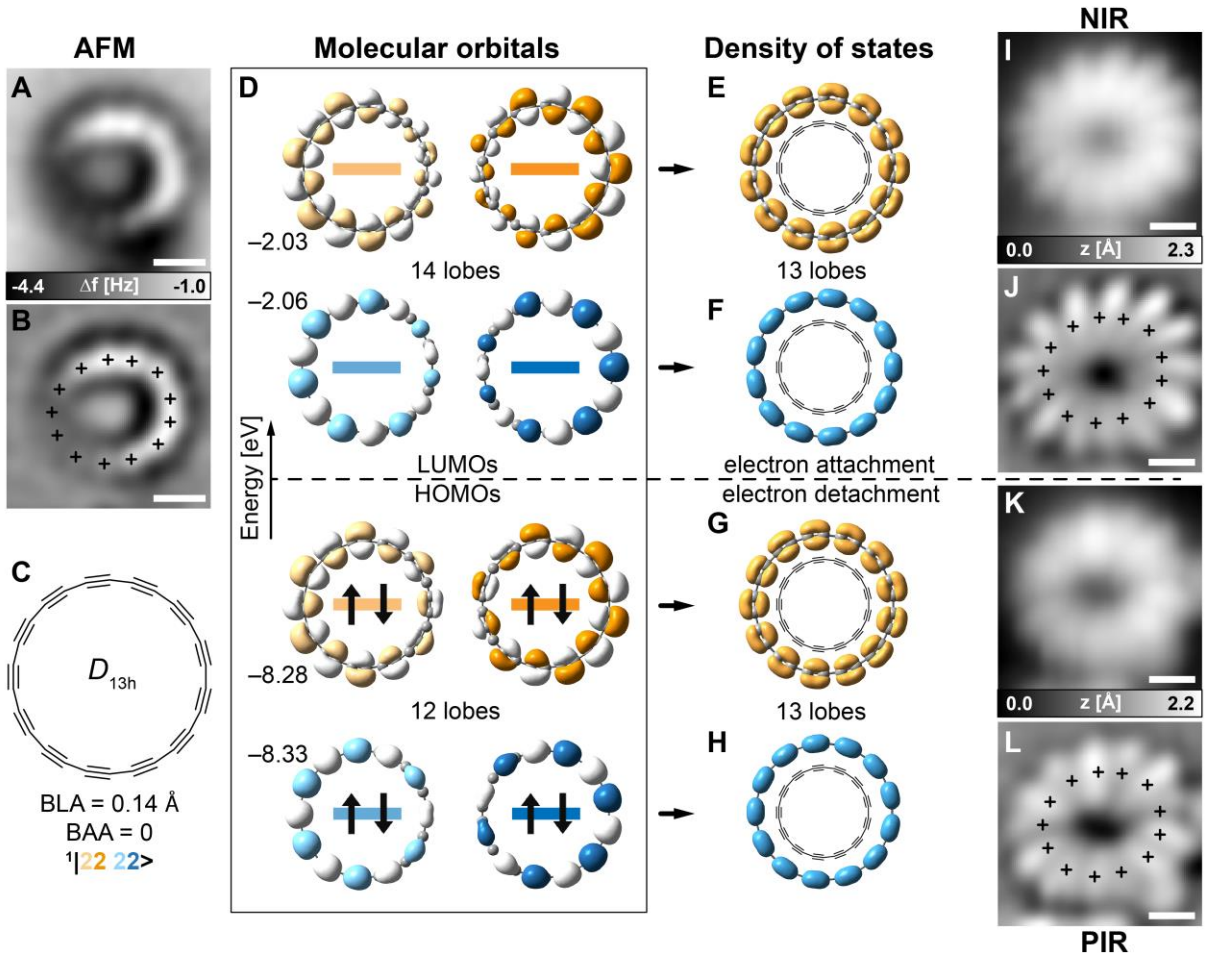

Fig. 4. Cyclo[26]carbon. (**A**) AFM data and (**B**) corresponding Laplace-filtered data, with the positions of the bright features, indicating short bonds, marked. (**C** to **H**) DFT calculations in the gas phase. (**D**) Frontier molecular orbitals, with energies in eV indicated. (**E** to **H**) Superposition of orbital densities of the respective energy degenerate orbital pairs shown in (D). (**I** and **J**) STM data at NIR, V = 2.0 V, I = 0.5 pA; (**K** and **L**) STM data at PIR, V = –2.75 V, I = 0.5 pA. (J and L) Laplace-filtered images of (I and K) with the positions of the short bonds, obtained by AFM (B), marked. Scale bars 5 Å.

Using STM, we resolved orbital densities of this (4k + 2) cyclocarbon (Fig. 4). In agreement with theory (Fig. 4, D to H), the STM maps for both NIR, imaged at V = 2.0 V (Fig. 4, I and J) and positive ion resonance (PIR) imaged at V = –2.75 V (Fig. 4, K and L), showed 13 lobes. For the NIR, the lobes of high density were located above the long bonds (between the marks in Fig. 4J), as expected from a superposition (*36*) of the energy-degenerate lowest unoccupied molecular orbitals (LUMOs), which have 14 lobes each (see Fig. 4F). For the PIR, the lobes were located above the short bonds (on the marks in Fig. 4L) and could result from the superposition of the densities of the energy-degenerate highest occupied molecular orbitals (HOMOs), see Fig. 4G. However, as explained above for the case of C_{13}, out-of-plane orbitals would dominate the STM contrast because they expose a larger orbital density toward the tip than the in-plane orbitals and are almost energy degenerate with them.

Like the in-plane HOMOs, the out-of-plane HOMOs (HOMO–2 and HOMO–3) of C_{26} have 12 lobes each, the superposition of which yields 13 lobes above short bonds (Fig. 4H). Tunnelling dominantly into the exposed out-of-plane HOMOs at the PIR explained why the cylindrical nodal plane along the ring of the in-plane HOMOs was not observed in the STM map of the PIR (Fig. 4, K and L), similar to measurements on C_{20} (*4*). The observation of the ionic resonances as superpositions of the densities of two orbitals resulted from the energy degeneracy of the respective two orbitals (*36*), and confirmed the doubly aromatic, closed-shell singlet configuration of C_{26}.

Generating a cyclocarbon by fusing two cyclocarbons or their precursors was to date not reported in on-surface experiments studying even-*N* cyclocarbons (*1-4*, *21*). The high reactivity of odd-*N* C_{13} probably makes it favorable for two C_{13} molecules to fuse and form C_{26}. The on-surface synthesis of C_{26} indicated that odd-*N* cyclocarbons and/or their precursors, because of their extremely high reactivity, allow the creation of larger novel carbon allotropes (*37*).

References

[1] Kaiser, K., Scriven, L. M., Schulz, F., Gawel, P., Gross, L., and Anderson, H. L. An *sp*-hybridized molecular carbon allotrope, cyclo[18]carbon. *Science* **365**, 1299–1301 (2019).

[2] Gao, Y., Albrecht, F., Rončević, I., Ettedgui, I., Kumar, P., Scriven, L. M., Christensen, K. E., Mishra, S., Righetti, L., Rossmannek, M., et al. On-surface synthesis of a doubly anti-aromatic carbon allotrope. *Nature* **623**, 977–981 (2023).

[3] Sun, L., Zheng, W., Gao, W., Kang, F., Zhao, M., and Xu, W. Aromatic annular carbon allotropes: cumulenic cyclo[10]carbon and Peierls-transition-intermediate cyclo[14]carbon. *Nature* **623**, 972–976 (2023).

[4] Sun, L., Zheng, W., Kang, F., Gao, W. and Xu, W., On-surface synthesis and characterization of anti-aromatic cyclo[12]carbon and cyclo[20]carbon, PREPRINT (Version 2) available at Research Square [https://doi.org/10.21203/rs.3.rs-3411934/v2] (2023)

[5] Diederich, F., Rubin, Y. Knobler, C. B., Whetten, R. L., Schriver, K. E., Houk, K. N., and Li, Y. All-carbon molecules: evidence for the generation of cyclo [18] carbon from a stable organic precursor. *Science* **245**, 1088–1090 (1989).

[6] Chen, X., Yan, X., Liu, Z., Yuan, T., Bu, C., Shang, Y., Xiao, H., Wu, Y., Wei, H., and Xu, J. Chemistry of cyclo-[2n]-carbon: A many-particle quantum mechanics investigation. *PREPRINT ChemRxiv 10.26434/chemrxiv-2023-plj1t-v2* (2023).

[7] Hoffmann, R. Extended Hückel theory — V: Cumulenes, polyenes, polyacetylenes and C_n. *Tetrahedron* **22**, 521–538 (1966).

[8] Hutter, J., Luethi, H. P., and Diederich, F. Structures and vibrational frequencies of the carbon molecules C2-C18 calculated by density functional theory. *J. Am. Chem. Soc.* **116**, 750–756 (1994).

[9] Fowler, P. W., Mizoguchi, N., Bean, D. E., and Havenith, R. W. A. Double aromaticity and ring currents in all-carbon rings. *Chem. Eur. J.* **15**, 6964–6972 (2009).

[10] Brito, B., Hai, G.-Q., and Cândido, L. Quantum Monte Carlo study on the structures and energetics of cyclic and linear carbon clusters C_n (n = 1,..., 10). *Phys. Rev. A* **98**, 062508 (2018).

[11] Yen, T. and Lai, S. Use of density functional theory method to calculate structures of neutral carbon clusters C_n ($3 \leq n \leq 24$) and study their variability of structural forms. *J. Chem. Phys.* **142**, 084313 (2015).

[12] Baryshnikov, G. V., Valiev, R. R., Nasibullin, R. T., Sundholm, D., Kurten, T., and Ågren, H. Aromaticity of even-number cyclo[*n*]carbons (n = 6–100). *J. Phys. Chem. A* **124**, 10849–10855 (2020).

[13] Baryshnikov, G. V., Valiev, R. R., Valiulina, L. I., Kurtsevich, A. E., Kurtén, T., Sundholm, D., Pittelkow, M., Zhang, J., and Ågren, H. Odd-number cyclo[*n*]carbons sustaining alternating aromaticity. *J. Phys. Chem. A* **126**, 2445–2452 (2022).

[14] Rončević, I., Leslie, F. J., Rossmannek, M., Tavernelli, I., Gross, L., and Anderson, H. L. Aromaticity reversal induced by vibrations in cyclo[16]carbon. *J. Am. Chem. Soc.* **145**, 26962–26972 (2023).

[15] Anderson, H. L., Patrick, C. W., Scriven, L. M., and Woltering, S. L. A short history of cyclocarbons. *Bull. Chem. Soc. Jpn.* **94**, 798–811 (2021).

[16] Tobe, Y. and Wakabayashi, T. Polyynes: synthesis, properties, and applications, Ch. 6, Ed. Cataldo, F., CRC Press (2005).

[17] Marlton, S. J., Buntine, J. T., Watkins, P., Liu, C., Jacovella, U., Carrascosa, E., Bull, J. N., and Bieske, E. J. Probing colossal carbon rings. *J. Phys. Chem. A* **127**, 1168–1178 (2023).

[18] Wang, S., Rittby, C., and Graham, W. Detection of cyclic carbon clusters. I. Isotopic study of the $\nu_4(e')$ mode of cyclic C_6 in solid Ar. *J. Chem. Phys.* **107**, 6032–6037 (1997).

[19] Clair, S. and de Oteyza, D. G. Controlling a chemical coupling reaction on a surface: tools and strategies for on-surface synthesis. *Chem. Rev.* **119**, 4717–4776 (2019).

[20] Gross, L., Mohn, F., Moll, N., Liljeroth, P., and Meyer, G. The Chemical Structure of a Molecule Resolved by Atomic Force Microscopy. *Science* **325**, 1110–1114 (2009).

[21] Scriven, L. M., Kaiser, K., Schulz, F., Sterling, A. J., Woltering, S. L., Gawel, P., Christensen, K. E., Anderson, H. L., and Gross, L. Synthesis of cyclo[18]carbon via debromination of $C_{18}Br_6$. *J. Am. Chem. Soc.* **142**, 12921–12924 (2020).

[22] Janssen, C. L., Schaefer III, H. F. Cycloheptatrienylidene singlet-triplet energetics: theory responds. *J. Am. Chem. Soc.* **109**, 5030–5031 (1987).

[23] Bofill, J. M., Bru, N., Farras, J., Olivella, S., Sole, A., Vilarrasa, J. Molecular and electronic structure of the low-lying electronic states of cycloalkenylidenes. Cyclopentadienylidene. *J. Am. Chem. Soc.* **110**, 3740–3746 (1988).

[24] S. Matzinger, T. Bally, E. V. Patterson, R. J. McMahon, The C_7H_6 potential energy surface revisited: Relative energies and IR assignment. *J. Am. Chem. Soc.* **118**, 1535–1542 (1996).

[25] Kassaee, M. Z., Arshadi, S., Acedy, M., Vessally, E. Singlet–triplet energy separations in divalent five-membered cyclic conjugated C_5H_3X, C_4H_3SiX, C_4H_3GeX, C_4H_3SnX, and $C4H_3PbX$ (X= H, F, Cl, and Br). *J. Organomet. Chem.* **690**, 3427–3439 (2005).

[26] Moreno-Armenta, M. G., Pearce, H. R., Winter, P., Cooksy A. L. Computational search for metastable high-spin C_5H_n (n = 4, 5, 6) species. *Comput. Theor. Chem.* **1140**, 1–6 (2018).

[27] Gross, L., Mohn, F., Moll, N., Schuler, B., Criado, A., Guitián, E., Peña, D., Gourdon, A., Meyer, G. Bond-Order Discrimination by Atomic Force Microscopy. *Science*. **337**, 1326–1329 (2012).

[28] Hapala, P, Kichin, G., Wagner, C., Tautz, F. S., Temirov, R. and Jelínek, P. The mechanism of high-resolution STM/AFM imaging with functionalized tips. *Phys. Rev. B*. **90**, 85421 (2014).

[29] Schuler, B., Fatayer, S., Mohn, F., Moll, N., Pavliček, N., Meyer, G., Peña, D. and Gross, L. Reversible Bergman cyclization by atomic manipulation. *Nat. Chem.* **8**, 220–224 (2016).

[30] Lee, J. K., Lee, G. D., Lee, S., Yoon, E., Anderson, H. L., Briggs, G. A. D., and Warner, J. H. Atomic scale imaging of reversible ring cyclization in graphene nanoconstrictions. *ACS Nano* **13**, 2379–2388 (2019).

[31] Pavliček, N., Schuler, B., Collazos, S., Moll, N., Pérez, D., Guitián, E., Meyer, G., Peña, D., and Gross, L. On-surface generation and imaging of arynes by atomic force microscopy. *Nat. Chem.* **7**, 623–628 (2015).

[32] Repp, J., Meyer, G., Stojkovic, S. M., Gourdon, A., and Joachim, C. Molecules on Insulating Films: Scanning-Tunneling Microscopy Imaging of Individual Molecular Orbitals. *Phys. Rev. Lett.* **94**, 026803 (2005).

[33] Szabo, A. and Ostlund, N. S. Modern Quantum Chemistry: Introduction to Advanced Electronic Structure Theory, McGraw-Hill Publishing Company, New York (1989).

[34] Pomogaev, V., Lee, S., Shaik, S., Filatov, M., and Choi, C. H. Exploring Dyson's orbitals and their electron binding energies for conceptualizing excited states from response methodology. *J. Phys. Chem. Lett.* **12**, 9963–9972 (2021).

[35] Ortiz, J. Dyson-orbital concepts for description of electrons in molecules. *J. Chem. Phys.* **153**, 070902 (2020).

[36] Pavliček, N., Mistry, A., Majzik, Z., Moll, N., Meyer, G., Fox, D. J., and Gross, L. Synthesis and characterization of triangulene. *Nat. Nano.* **12**, 308–311 (2017).

[37] Diederich, F. Carbon scaffolding: building acetylenic all-carbon and carbon-rich compounds. *Nature* **369**, 199–207 (1994).

[38] Zenodo dataset: Computational data for The odd-number cyclo[13]carbon and its dimer cyclo[26]carbon. DOI: 10.5281/zenodo.10526999.

[39] Giessibl, F. J. Atomic resolution on *Si*(111)-7×7 by noncontact atomic force microscopy with a force sensor based on a quartz tuning fork. *Appl. Phys. Lett.* **76**, 1470–1472 (2000).

[40] Albrecht, T. R., Grütter, P., Horne, D., and Rugar, D. Frequency modulation detection using high-Q cantilevers for enhanced force microscope sensitivity. *J. Appl. Phys.* **69**, 668–673 (1991).

[41] Fdez. Galván, I. et al. OpenMolcas: From source code to insight. *J. Chem. Theory. Comput*. **15**, 5925–5964 (2019).

[42] Kendall, R. A., Dunning Jr, T. H., and Harrison, R. J. Electron affinities of the first-row atoms revisited. Systematic basis sets and wave functions. *J. Chem. Phys*. **96**, 6796–6806 (1992).

[43] Finley, J., Malmqvist, P.-Å., Roos, B. O., and Serrano-Andrés, L. The multi-state CASPT2 method. *Chem. Phys. Lett.* **288**, 299–306 (1998).

[44] Chai, J. D. and Head-Gordon, M. Long-range corrected hybrid density functionals with damped atom–atom dispersion corrections. *Phys. Chem. Chem. Phys.* **10**, 6615–6620 (2008).

[45] Weigend, F. and Ahlrichs, R. Balanced basis sets of split valence, triple zeta valence and quadruple zeta valence quality for H to Rn: Design and assessment of accuracy. *Phys. Chem. Chem. Phys.* **7**, 3297–3305 (2005).

[46] Frisch, M. J. et al. Gaussian 16 Rev. C.01, Wallingford, CT (2016).

[47] Martin, C. W., Gill, H. S. and Landgrebe, J. A. Diaryldichlorocarbonyl ylides derived from dichlorocarbene and aromatic ketones. *J. Org. Chem.* **48**, 1898–1901 (1983).

[48] Soya, T., Mori, H. and Osuka, A. Quadruply twisted Hückel-aromatic dodecaphyrin. *Angew. Chem. Int. Ed.* **57**, 15882 (2018).

[49] Li Manni, G., Fdez. Galvan I. *et al.*, The OpenMolcas Web: A Community-Driven Approach to Advancing Computational Chemistry. *J. Chem. Theory Comput.* **19**, 6933 (2023).

[50] Ibe Y., Nakagawa Y. O., Earnest N., Yamamoto T., Mitarai K., Gao Q., and Kobayashi T. Calculating transition amplitudes by variational quantum deflation. *Phys. Rev. Res.* **4**, 013173 (2021).

[51] Oana, C. M., and Krylov A. I., Dyson orbitals for ionization from the ground and electronically excited states within equation-of-motion coupled-cluster formalism: Theory, implementation, and examples. *J. Chem. Phys.* **127**, 234106 (2007).

[52] Guo, Y., Riplinger, C., Becker, U., Liakos, D. G., Minenkov, Y., Cavallo, L., Neese, F. Communication: An improved linear scaling perturbative triples correction for the domain based local pair-natural orbital based singles and doubles coupled cluster method [DLPNO-CCSD(T)]. *J. Chem. Phys.* **148**, 011101 (2018).

[53] Hättig, C., Klopper, W., Köhn, A., Tew, D. P. Explicitly correlated electrons in molecules. *Chem. Rev.* **112**, 4-74 (2012).

[54] Kong, L., Bischoff, F. A., Valeev, E. F. Explicitly correlated R12/F12 methods for electronic structure. *Chem. Rev.* **112**, 75-107 (2012).

[55] Neese, F., Wennmohs, F., Becker, U., Riplinger, C. The ORCA quantum chemistry program package. *J. Chem. Phys.* **152**, 224108 (2020).

[56] Monaco, G., Summa, F. F., and Zanasi, R. Program package for the calculation of origin-independent electron current density and derived magnetic properties in molecular systems. *J. Chem. Inf. Model.* **61**, 270-283 (2021).

Acknowledgments: We thank Marcin Majewski for discussions.

Funding: European Research Council grant 885606, ARO-MAT (HLA, YG).

European Community Horizon 2020, grant project 101019310 CycloCarbonCatenane (YG, HLA).

UKRI Horizon Europe Guarantee MSCA Postdoctoral Fellowship ElDelPath, EP/X030075/1 (IR, HLA).

European Research Council Synergy grant 951519, MolDAM.

European Union project SPRING, grant 863098.

Computational resources were provided by Cirrus UK National Tier-2 HPC Service at EPCC (http://www.cirrus.ac.uk) funded by the University of Edinburgh and EPSRC (EP/P020267/1); Ministry of Education, Youth and Sports of the Czech Republic through the e-INFRA CZ (ID:90140).

Author contributions: Conceptualization: FA, HLA, LG

Synthesis of the precursors: YG

On-surface synthesis and STM/AFM measurements: FA, FP, SM, LG

Theoretical analysis and computational simulations: IR, AB, IT

Writing: All authors.

Competing interests: The authors declare that they have no competing interests.

Data and materials availability: All experimental data are reported in the main text and supplementary materials. Additional data, i.e., results of calculations, are deposited at Zenodo: 10.5281/zenodo.10526999.

Supplementary Materials

Materials and Methods

Supplementary Text

Figs. S1 to S25

References (*39*-*56*)

Supplementary Material for

The odd-number cyclo[13]carbon and its dimer cyclo[26]carbon

Florian Albrecht,[1†] Igor Rončević,[2†] Yueze Gao[2†], Fabian Paschke[1†], Alberto Baiardi[3], Ivano Tavernelli[3], Shantanu Mishra[1], Harry L. Anderson[2]* and Leo Gross[1]*

[1] IBM Research Europe – Zürich, 8803 Rüschlikon, Switzerland.

[2] Department of Chemistry, Oxford University, Chemistry Research Laboratory, Oxford, United Kingdom.

[3] IBM Quantum, IBM Research Europe – Zürich, 8803 Rüschlikon, Switzerland.

† These authors contributed equally.

*Corresponding authors. Email: harry.anderson@chem.ox.ac.uk; lgr@zurich.ibm.com

Contents

1. STM and AFM methods

The on-surface characterization and reactions were performed in a home-built combined STM/AFM, operated at a temperature of 5 Kelvin in ultra-high vacuum. The precursor, i.e., decachlorofluorene, was thermally sublimed onto a cold (T < 10 K) Au(111) surface partially covered with NaCl islands of one (ML) and two (BL) atomic layers thickness. AFM measurements were performed in non-contact mode with a qPlus sensor (*39*). The sensor was operated in frequency modulation mode (*40*) with the oscillation amplitude kept constant at 0.5 Å. If not noted otherwise, all data were recorded on molecules adsorbed on ML NaCl on Au(111) with CO functionalized tips. STM images were recorded at constant current and AFM images at constant height. The STM controlled setpoint for constant-height AFM images was I = 1.0 pA and V = 0.2 V if not mentioned otherwise. Positive (negative) tip-height offsets Δz correspond to an increase (decrease) in tip-sample distance with respect to the setpoint. In the AFM images of the intermediates, shown in Fig. 1, Δz was selected to result in bond resolved contrast. Typically, that is achieved at a maximal frequency shift Δf of about 0 Hz in the AFM image. With AFM-far we denote an imaging height (Δz) just at the onset of atomic resolution. That is, Δz chosen as large as possible to still yield bond resolved contrast. With AFM-close, we denote imaging at Δz further reduced by about 0.3 Å, with respect to AFM-far. At AFM-far, bond-order related contrast is usually observed as brightness contrast in the Δf-map, while at AFM close, due to CO-tip relaxations (*27, 28*), bond-order related contrast is observed in the apparent bond length (27). The latter results in apparent corners at the position of triple bonds in polyynic cyclocarbons (*1, 21*). AFM images were acquired at V = 0 V. The bias voltage V was applied to the sample with respect to the tip.

Voltage pulses to induce dehalogenation, typically with V = 4.3 to 4.5 V were applied at constant height for a few 100 ms, with the tip being retracted by 6 to 8 Å from a setpoint of I = 1 pA and V = 0.2 V, resulting in currents I on the order of few pA. With such pulses the yield for generating C_{13} was about 40%, (25 successful events versus 38 unsuccessful attempts, see fig. S10 for examples of the latter). In the successful events, C_{13} was formed with one or few of such pulses from an individual precursor, dissociating several Cl atoms from the precursor with one pulse. Using pulses with smaller voltages and smaller currents, fewer Cl atoms were dissociated by an individual pulse. However, the yield for generating C_{13} by multiple of such smaller voltage and/or smaller current pulses was small. The investigation of the yield and the specific intermediates formed as a function of the pulse values, and the systematic optimization of the yield as a function of the pulse parameters, is out of the scope of this work.

2. Computational methods

All multireference calculations were done using OpenMolcas (*41*). The geometry of C_{13} was optimized at the CASPT2(6,8)/cc-PVTZ level of theory (*42*), which included all k = 3 (six lobes) and k = 4 (eight lobes) orbitals in the active space. We targeted the first triplet root, and both lowest singlets in a state-averaged two-state calculation. In the gas phase, the major contributions to the lowest triplet and singlet were both |21 21>, giving very similar round geometries (Fig. 3C), while the second singlet state, ^{1}|22 20>, optimized to a strongly kinked geometry (Fig. 3D). The (100) NaCl surface was simulated with an array of immobile point charges with a lattice parameter of 2.72 Å, following prior work (*2*). On each of the

calculated surfaces (Fig. 3, E to G), we found very similar relaxed geometries of C_{13} in its different electronic states, respectively. This indicates that on-surface geometries depend more strongly on the surface environment than on the chosen electronic state.

Single-point energies of optimized geometries were evaluated at the multistate (*43*) CASPT2(12,14)/cc-PVTZ with four states; for the anions, the (13,14) space was used. This active space captures all $\Delta k = 0$ and $\Delta k = \pm 1$ transitions involving frontier orbitals (*14*) and it was used in previous investigations of C_{13} (*13*).

The geometry minimum and electronic structure of C_{26}, as well as the aromaticity of C_{13}, was calculated at ωB97XD/def2-TZVP (*44, 45*), following prior work (*12, 13*), using the Gaussian16 program (*46*).

3. Synthetic general methods

Reagents were purchased reagent-grade from commercial suppliers and used without further purification. $MgSO_4$ was used as the drying reagent after the aqueous work-up. Thin layer chromatography (TLC) was carried out on aluminium-backed silica gel plates with 0.2 mm thick silica gel 60 F254 (Merck) and visualized via UV-light (254/364 nm). Flash column chromatography was either carried out using flash silica gel 60 (230-400 mesh) obtained from Sigma-Aldrich. ^{1}H and ^{13}C NMR spectra were recorded on Bruker AVIII HD 500 spectrometers at 500 MHz (^{1}H) and 126 MHz (^{13}C) at 298 K. NMR chemical shifts are reported in ppm relative to $SiMe_4$ ($\delta = 0$) and were referenced internally with respect to residual solvent protons using the reported values (^{1}H: $CDCl_3$: 7.26 ppm; ^{13}C: $CDCl_3$: 77.16 ppm). All chemical shifts are reported in ppm, coupling constants are reported in Hz and ^{1}H multiplicities are reported in accordance with the following: s = singlet; d = doublet; t = triplet; and m = multiplet.

Synthetic protocols:

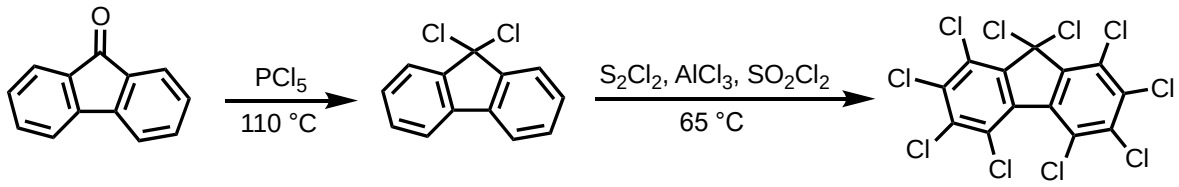

9,9-Dichlorfluorene. (*47*) 9H-Fluoren-9-one (1.00 g, 5.55 mmol) and PCl_5 (1.73 g, 8.32 mmol) were mixed and stirred at 110 °C for 16 hours. After cooling to room temperature, CH_2Cl_2 (30 mL) was added. The reaction mixture was quenched by slowly adding aqueous saturated Na_2CO_3 solution (20 mL) at 0 °C. H_2O (20 mL) was added, the layers were separated, and the aqueous phase was extracted with CH_2Cl_2 (2 × 40 mL). The organic phases were combined, washed with brine (20 mL), dried ($MgSO_4$), and filtered. Solvent removal and purification by recrystallization (diethyl ether) afforded **9,9-dichlorfluorene** (340 mg, 1.45 mmol, 26%) as a white solid. **^{1}H NMR** (500 MHz, $CDCl_3$) δ 7.84–7.82 (m, 1H), 7.62–7.60 (m, 1H), 7.45–7.39 (m, 2H). **^{13}C NMR** (126 MHz, $CDCl_3$) δ 146.9, 136.7, 130.8, 129.2, 124.8, 120.3, 83.1.

Decachlorofluorene. To a suspension of $AlCl_3$ (851 mg, 6.38 mmol) in SO_2Cl_2 (75 mL) was added a solution of 9,9-dichlorfluorene (100 mg, 0.425 mmol) in S_2Cl_2 (2.0 mL, 25 mmol) and SO_2Cl_2 (25 mL) over 20 min via a syringe pump. In the meantime, the solution was stirred at 65 °C. After the completion of the addition, the solution was stirred at 65 °C for 16

h. After cooling to room temperature, CH_2Cl_2 (30 mL) was added. The mixture was slowly added into water at 0 °C, followed by quenching with aqueous saturated Na_2CO_3 solution (ca. 300 mL). The layers were separated, and the aqueous phase was extracted with CH_2Cl_2 (2 × 150 mL). The organic phases were combined, washed with brine (20 mL), dried ($MgSO_4$), and filtered. Solvent removal and washing with CH_2Cl_2 (8 mL) afforded decachlorofluorene as a white powder. The solvent was removed from the residual solution and the resulting solid was washed with diethyl ether (20 mL). These two batches of decachlorofluorene (180 mg, 0.352 mmol, 83%) were combined as a white powder. **^{1}H NMR** (500 MHz, $CDCl_3$) No signals from the product were observed. **^{13}C NMR** (126 MHz, $CDCl_3$) δ 142.2, 138.0, 136.5, 133.4, 130.6, 127.5, 81.1.

4. NMR Spectra

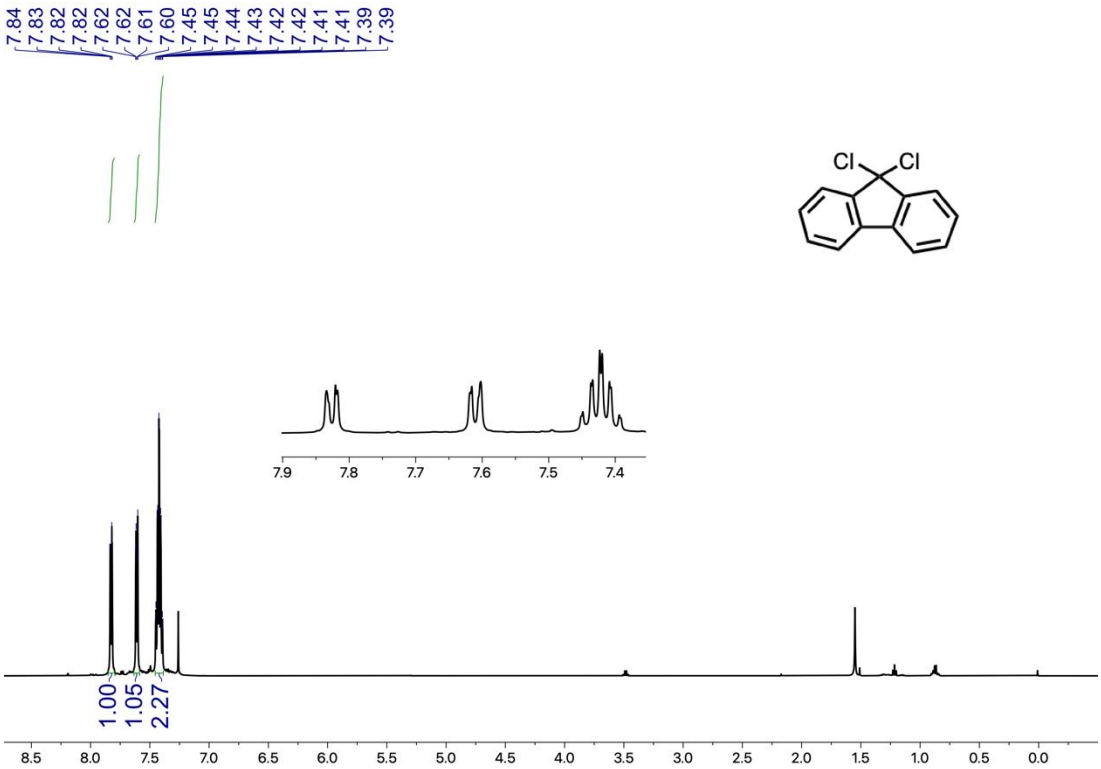

Figure S1. ^{1}H NMR (500 MHz) spectrum of compound 9,9-dichlorfluorene in $CDCl_3$.

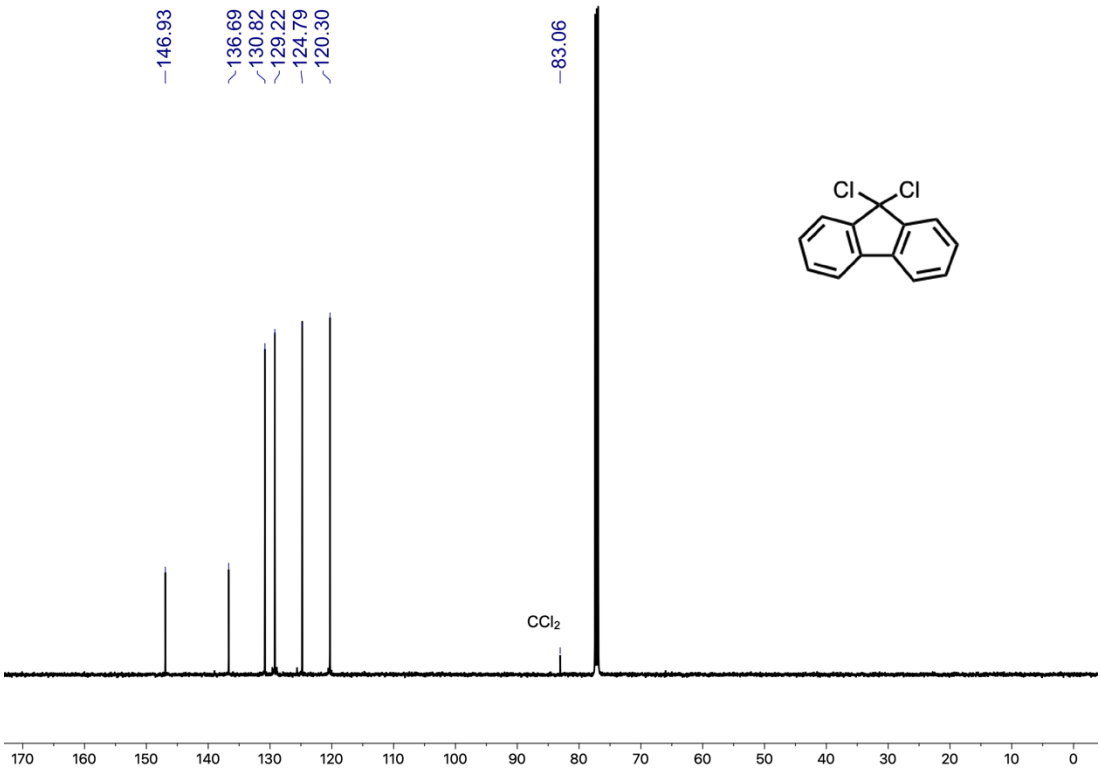

Figure S2. ^{13}C NMR (126 MHz) spectrum of compound 9,9-dichlorfluorene in $CDCl_3$.

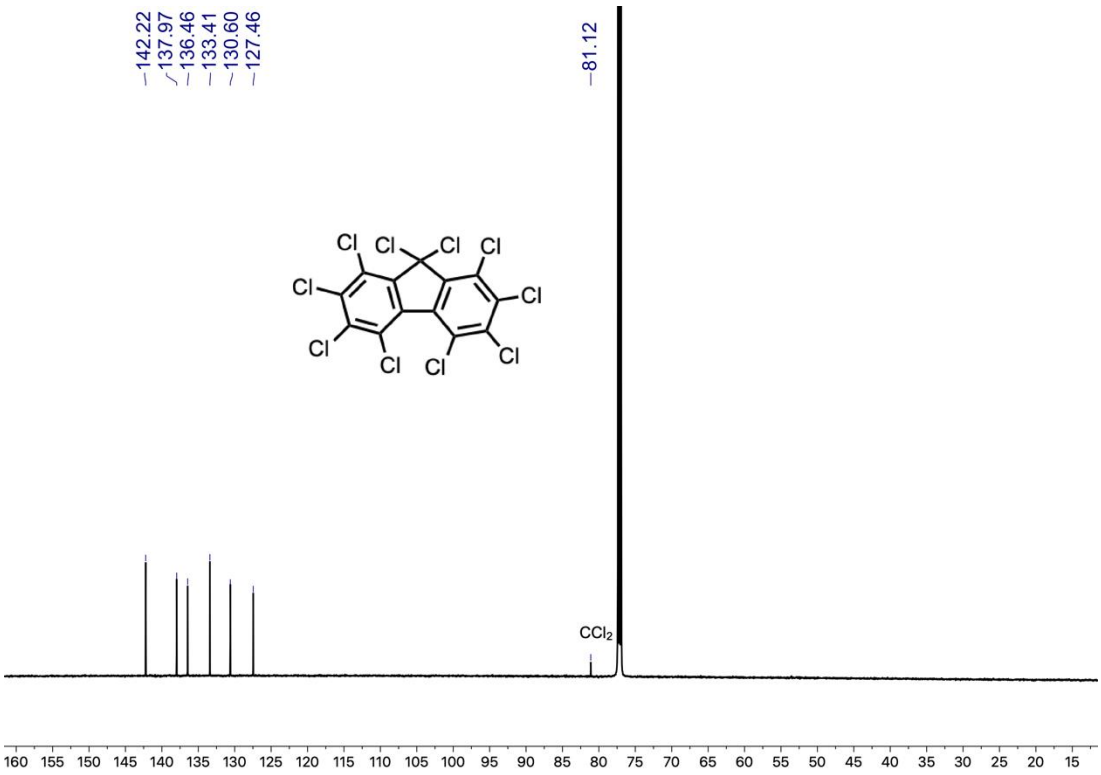

Figure S3. ^{13}C NMR (126 MHz) spectrum of compound decachlorofluorene in $CDCl_3$.

5. Additional experimental data on C_{13}

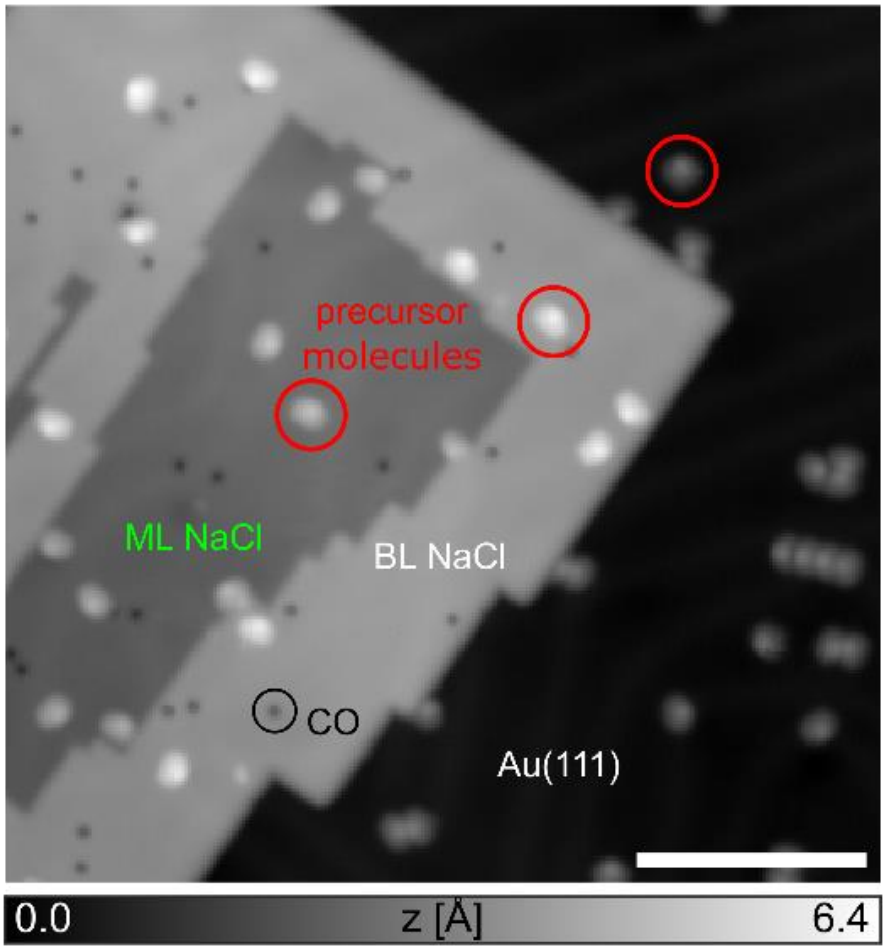

Figure S4. **STM overview image** (V = 0.2 V, I = 0.5 pA). A CO molecule, decachlorofluorene molecules (precursor molecules for C_{13}), areas of bilayer (BL) NaCl, monolayer (ML) NaCl, and the uncovered Au(111) surface are indicated. Scale bar 100 Å.

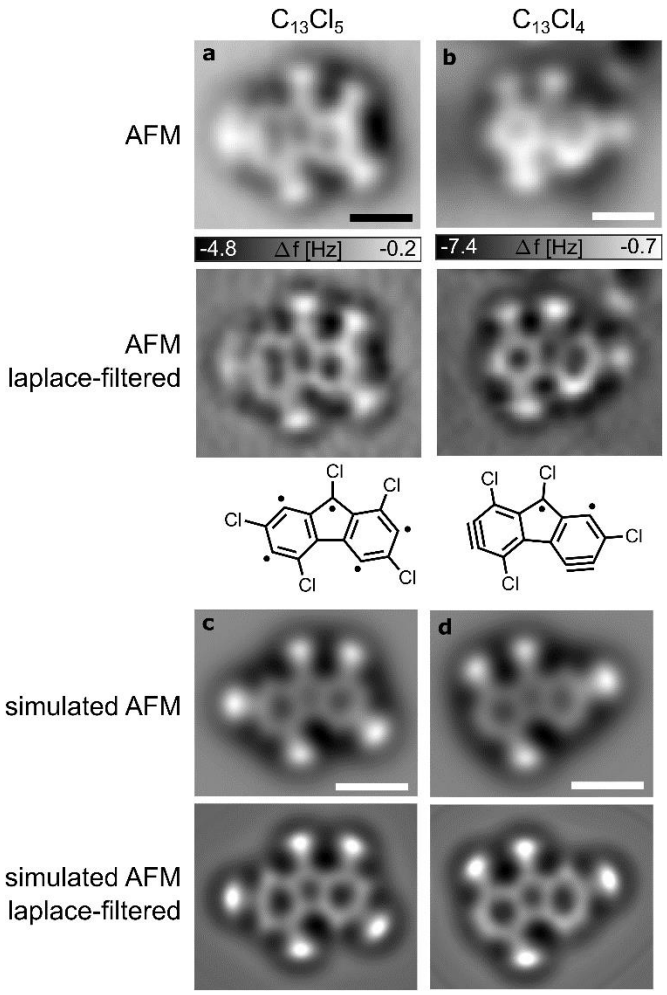

Figure S5. **AFM images of intermediates and AFM simulations. (a, b)** AFM data of intermediates as displayed in Fig. 2 D and E. **(c, d)** Simulated AFM images of proposed structures and corresponding Laplace-filtered images. Simulations of AFM images were performed based on DFT calculated xyz geometries using the Probe-Particle Model (*28*) with default CO-tip parameters (stiffness $k_x = k_y = 0.25$ N/m, $k_R = 30$ N/m) at an oscillation amplitude $A = 0.5$ Å. Scale bars 5 Å. Note that the apparent expansion of the carbon skeleton is increased near dechlorinated sites, most pronounced at the six-membered ring on the right hand side in (b) and (d). This effect is explained by the tilting of the CO at the tip towards the molecule at its periphery (*27*, *28*). That the effect is qualitatively reproduced in the Probe-Particle Model simulations, which take into account CO-tip relaxations, corroborates this explanation.

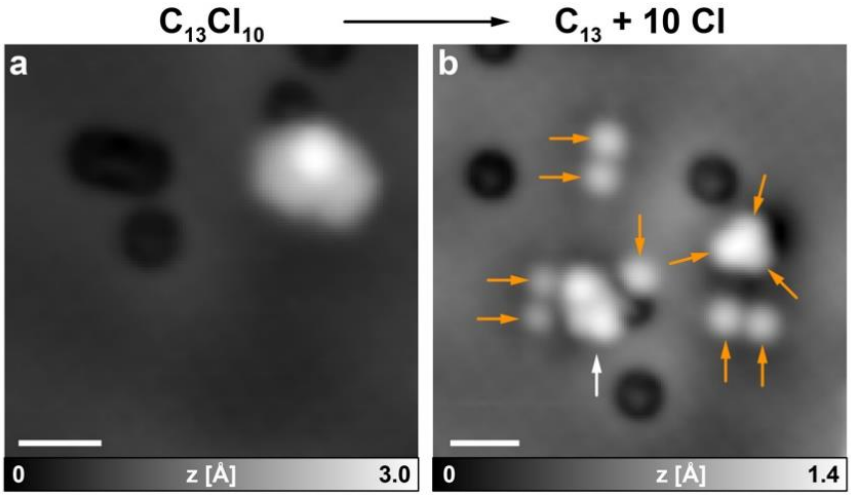

Figure S6. **STM images of C_{13} formation and dissociated chlorine atoms. (a)** STM image of individual precursor molecule adsorbed on ML NaCl next to a CO molecule. **(b)** After applying a voltage pulse of $V = 4.5$ V above the molecule shown in (a), with tip retracted by $\Delta z = 8$ Å from $V = 0.2$ V and $I = 1$ pA. The generated C_{13} is indicated by a white arrow, the ten dissociated chlorine atoms are indicated by orange arrows. Imaging parameters for both panels: $V = 0.2$ V, $I = 1$ pA. Scale bars 10 Å.

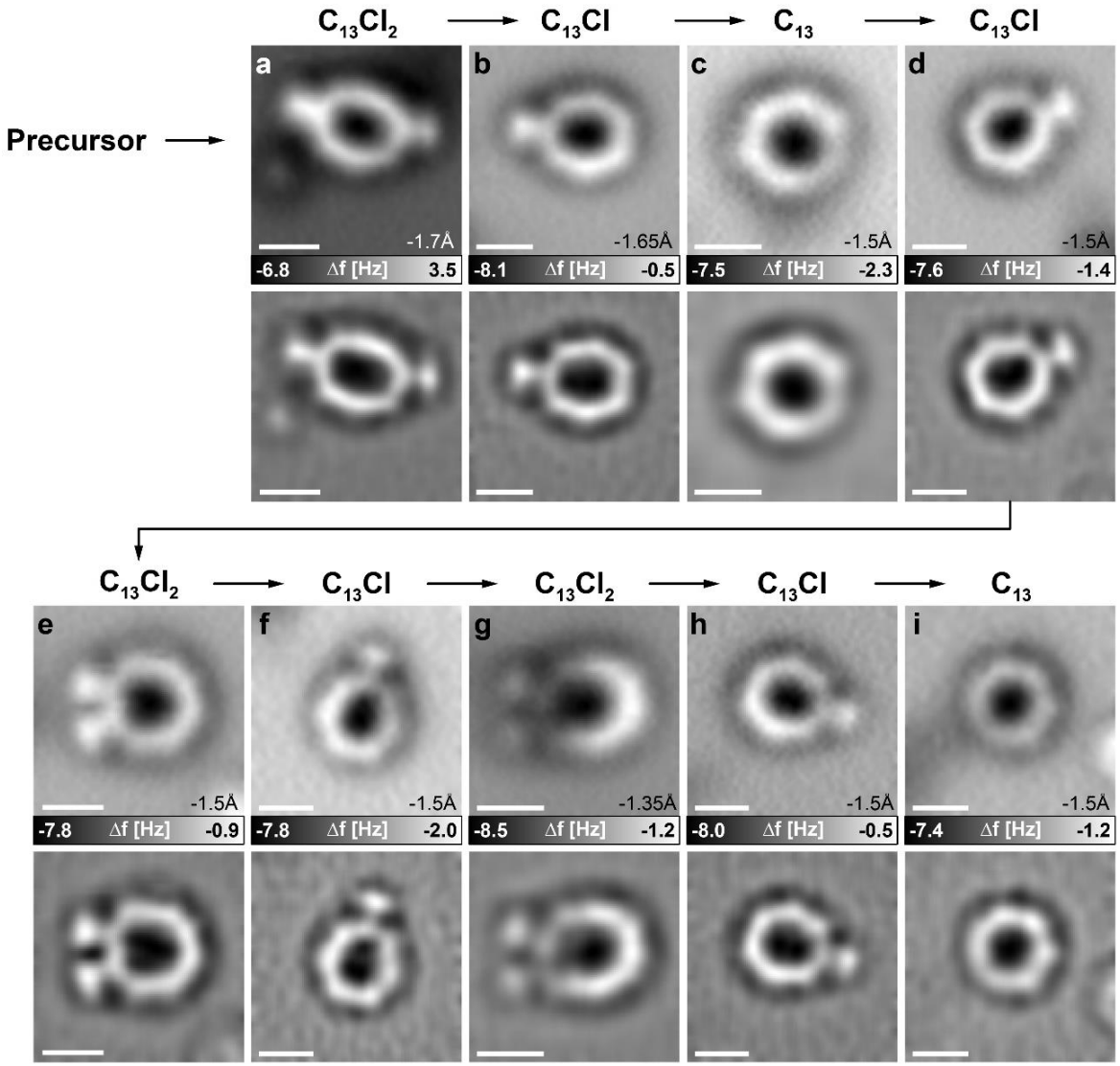

Figure S7. **Chlorination of a C_{13}.** AFM raw data (top) and corresponding Laplace-filtered images (bottom). Sequence of AFM images with voltage pulses (V = 4 to 4.5 V) applied above the molecule. (**a-c**) Dechlorination of $C_{13}Cl_2$ to C_{13}. (**c-e**) Chlorination of C_{13} to $C_{13}Cl_2$. (**e**, **f**) Dechlorination of $C_{13}Cl_2$ to C13Cl. (**f**, **g**) Chlorination of $C_{13}Cl$ to $C_{13}Cl_2$. (**g-j**) Dechlorination of $C_{13}Cl_2$ to C_{13}. Indicated tip-height offsets Δz refer to a setpoint of V = 0.2 V, I = 0.5 pA, Scale bars 5 Å. Up to two Cl atoms, adsorbed near C_{13} on the NaCl surface, could reversibly be reattached to C_{13}.

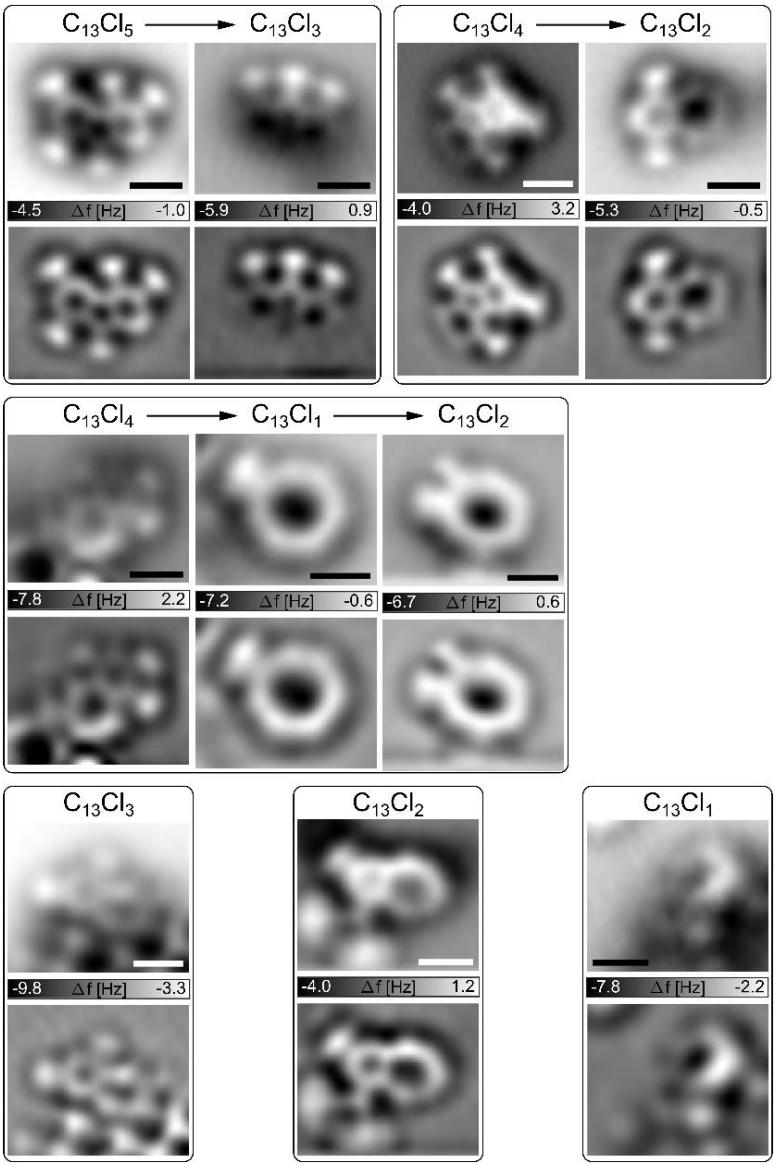

Figure S8. **Intermediates converted into C_{13}.** AFM images of intermediates generated from decachlorofluorene by voltage pulses. Further voltage pulses on these intermediates resulted in cyclo[13]carbon. Each respective lower panel shows Laplace-filtered data. Boxes are drawn around measurements of intermediates that resulted from a specific individual precursor. Scale bars 5 Å.

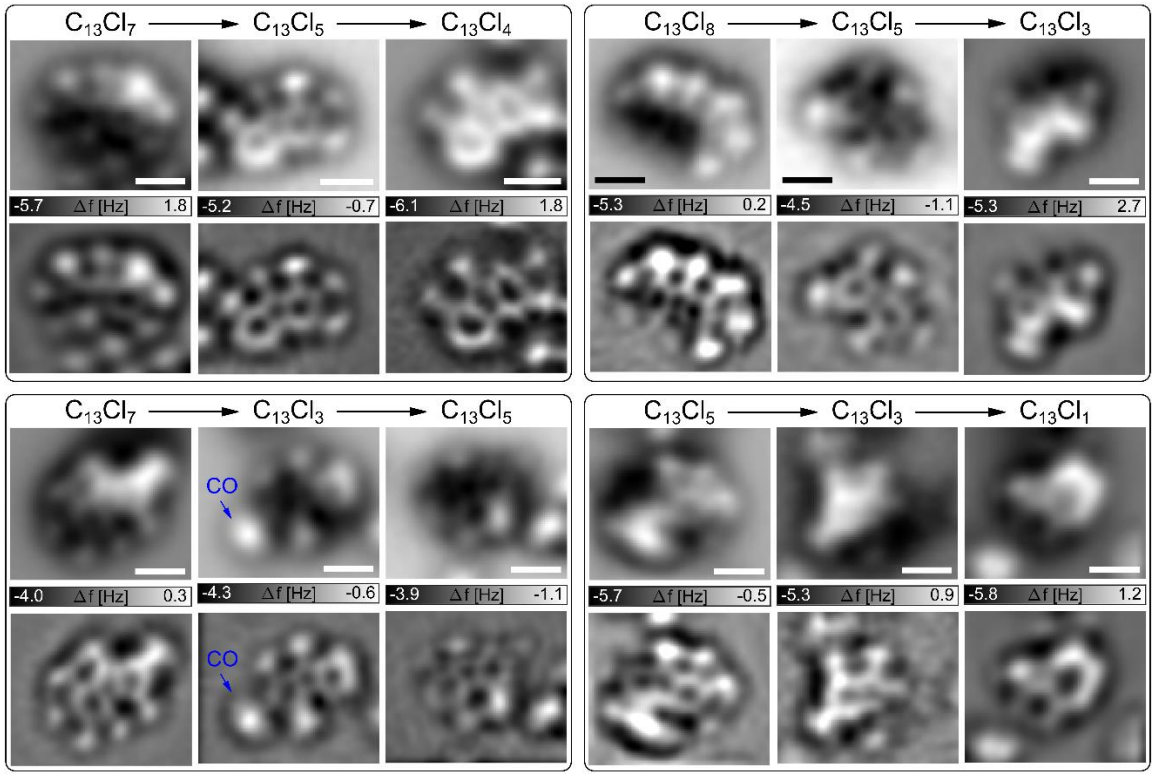

Figure S9. Intermediates not converted into C_{13}. AFM images of intermediates generated from decachlorofluorene by voltage pulses. Further voltage pulses on these intermediates did not result in cyclo[13]carbon, see fig. S10 for structures observed in instances of unsuccessful generation of C_{13}. Each respective lower panel shows Laplace-filtered data. Boxes are drawn around measurements of intermediates that resulted from a specific individual precursor. Scale bars 5 Å.

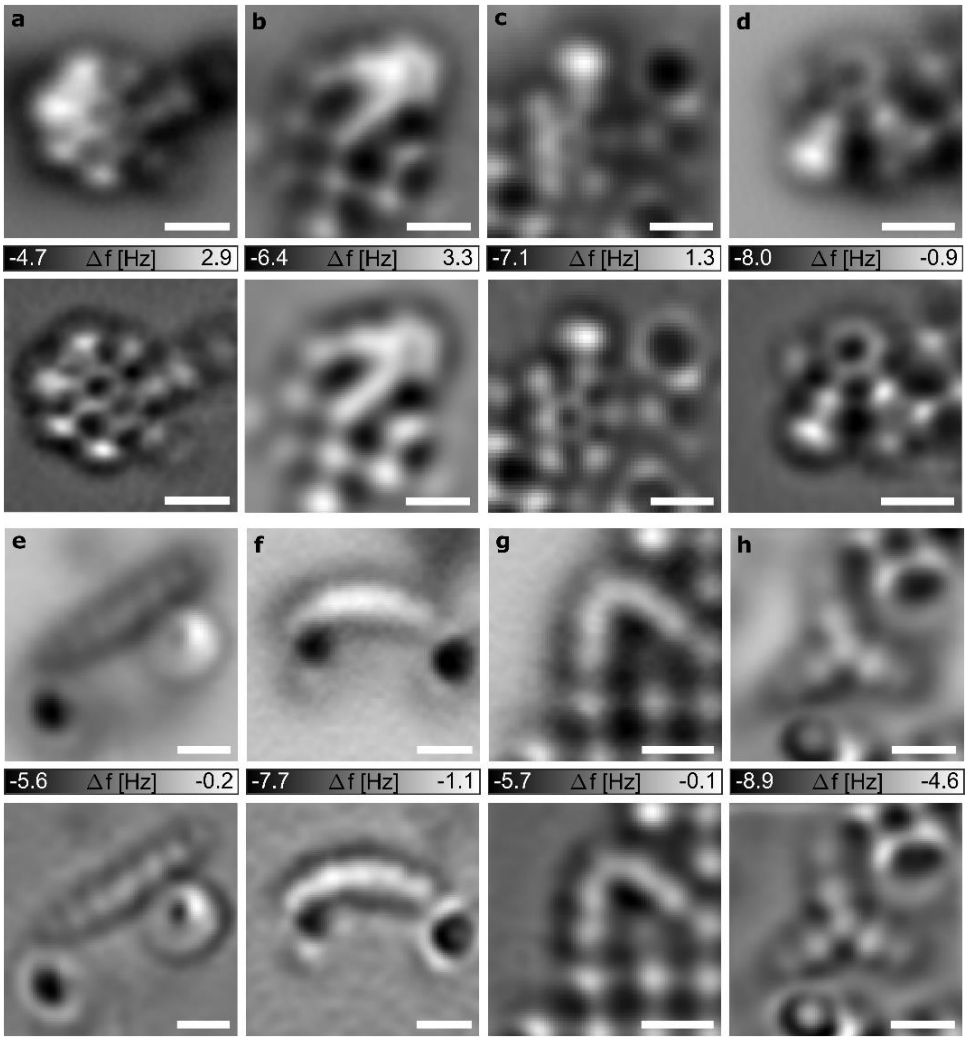

Figure S10. Unsuccessful results of attempted on-surface synthesis of C_{13}. Molecules observed after voltage pulses applied above decachlorofluorene that did not yield C_{13}. For each molecule (**a-h**), the AFM raw data is shown in the top panel and a corresponding Laplace-filtered image in the panel below. Molecules shown in (a, b, d, g) where adsorbed on bilayer NaCl, all other molecules on monolayer NaCl. We attempted generation of C_{13} on 63 individual decachlorofluorene precursors and successfully generated 25 individual C_{13} molecules resulting in a yield of about 40% for the on-surface synthesis. Scale bars 5 Å.

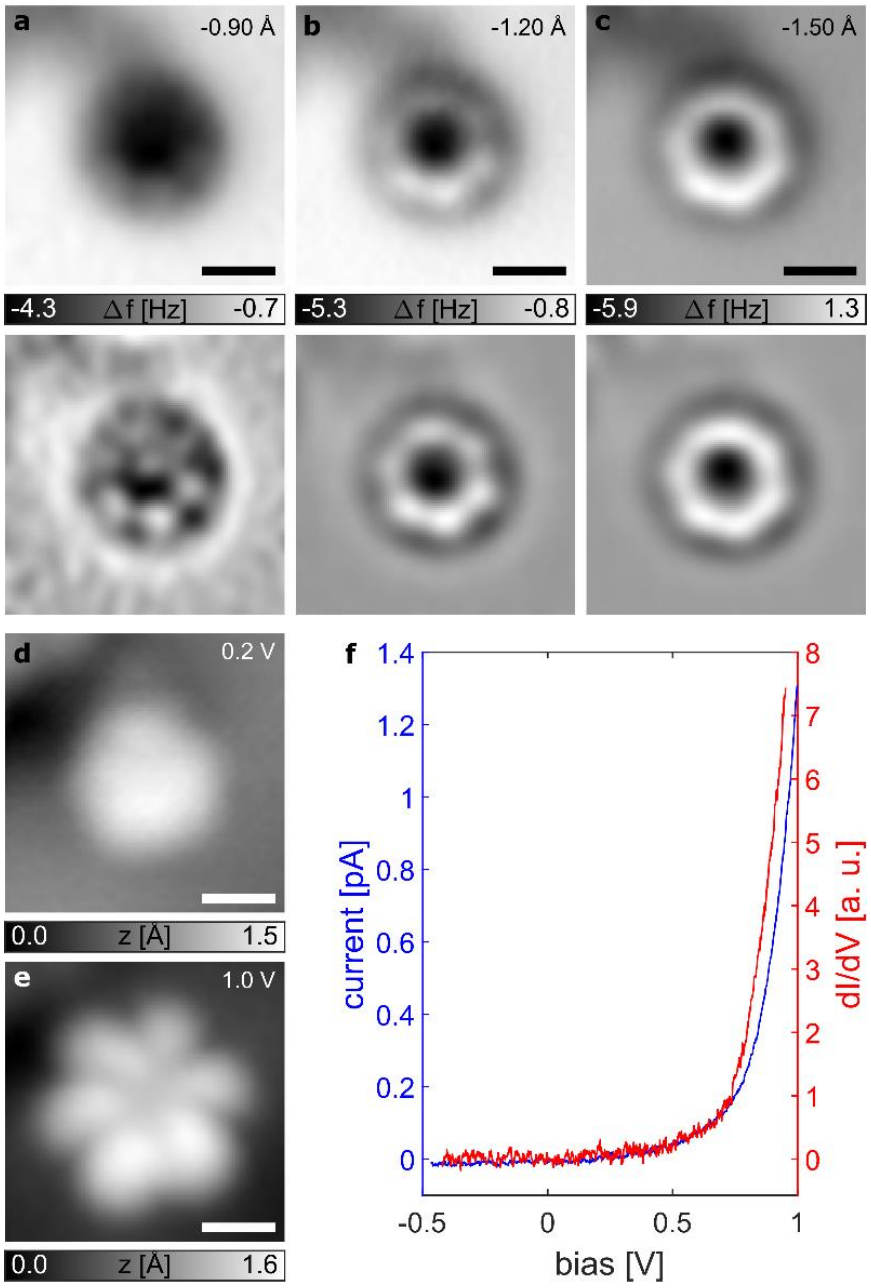

Figure S11. **Structural and electronic characterization of a "round" C_{13} on ML NaCl.** (**a-c**) AFM raw data and corresponding Laplace-filtered images below. Indicated tip-height offsets Δ*z* refer to a setpoint of $V = 0.2$ V, $I = 0.3$ pA. (**d, e**) Constant-current STM images recorded at indicated voltages, $I = 0.3$ pA. (**f**) $I(V)$ spectrum (blue) and numerically derived dI/dV spectrum (red). All scale bars 5 Å.

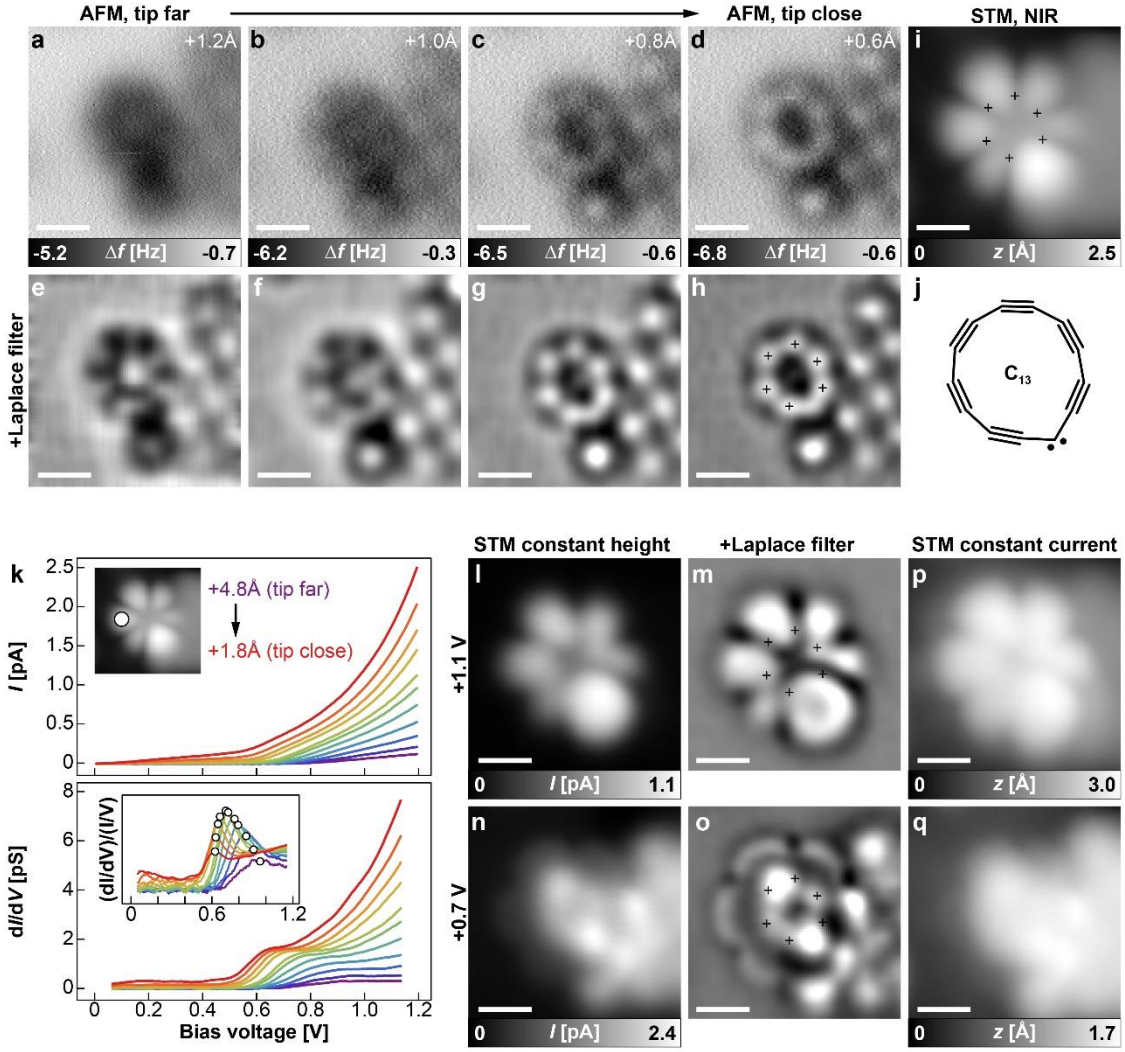

Figure S12. **Structural and electronic characterization of a "kinked" C_{13} on BL NaCl.** (**a-d**) AFM raw data and (**e-h**) corresponding Laplace-filtered images. C_{13} was stabilized at a third layer NaCl step edge. Indicated tip-height offsets Δz refer to a setpoint of V = 0.2 V, I = 1.0 pA on BL NaCl. (h) is displayed in Fig. 3H, rotated by 180 degrees to show the molecule in a similar orientation as in the corresponding calculations. (**i**) Constant-current STM image of the NIR recorded at V = +0.8 V and I = 1.0 pA. Crosses mark the bright spots in AFM-close, i.e., short bonds. (**j**) Corresponding orientation of the C_{13} on the surface. (**k**) $I(V)$ (top) and corresponding differential conductance dI/dV curves (bottom) recorded at the marked spot in the upper inset. Different tip heights are color-coded. Resonances in the dI/dV curves are highlighted by normalization on I/V (lower inset), and the peak positions are marked by circles. At larger tip heights (tip far), only one resonance at V_1 = +1.1 V is visible, whereas a second resonance appears upon tip approach (tip close), at about V_2 = +0.7 V. (**l-o**) Constant-height STM data (l, n) and Laplace-filtered images (m, o, displayed in Fig. 3L, rotated by 180 degrees) recorded at resonances V_1 (l, m) and V_2 (n, o). The tip-height offsets Δz are +4.2 Å (top) and +1.8 Å (bottom) from a setpoint of V = 0.2 V, I = 1.0 pA on BL NaCl. Whereas V_1 depicts an out-of-plane orbital, the image at V_2 appears to be an in-plane-orbital. (**p**, **q**) Corresponding constant-current STM data, I = 1.0 pA. All scale bars are 5 Å.

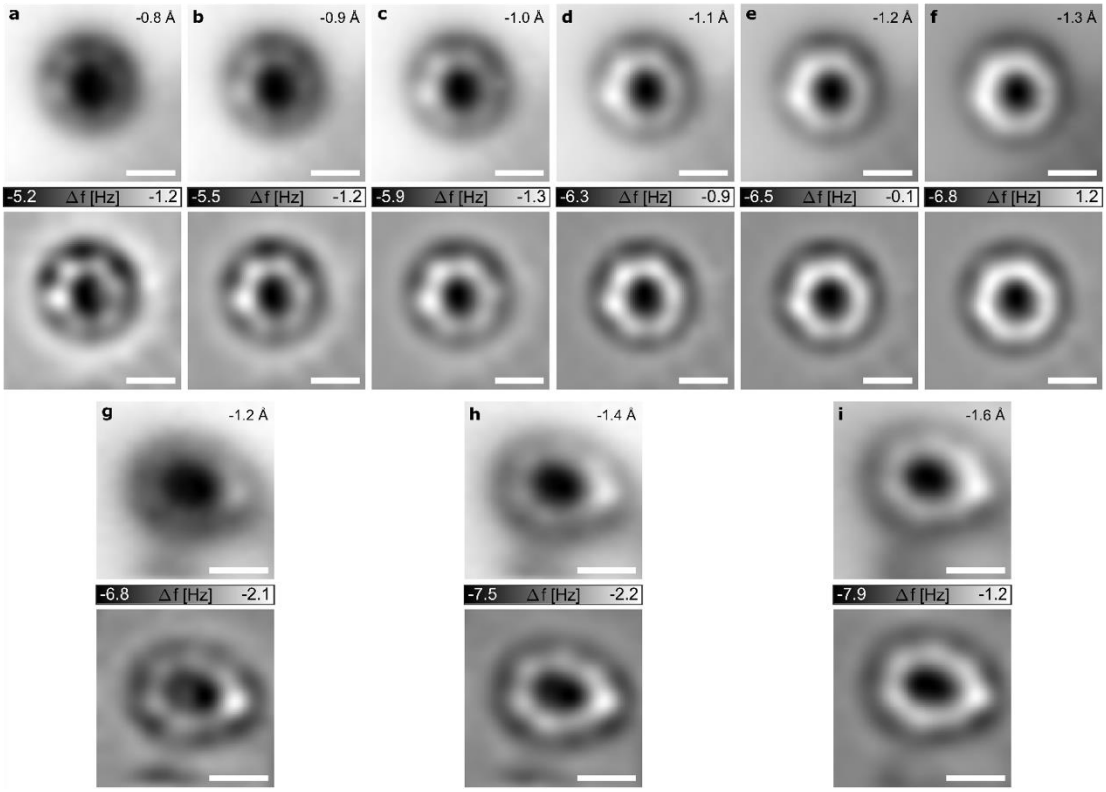

Figure S13. Additional AFM data on C_{13}. AFM images of a "round" (**a–f**) and a "kinked" (**g–i**) C_{13} molecule on ML NaCl. Raw AFM data is shown in upper panels and Laplace-filtered data is shown in the respective lower panels. Indicated tip-height offsets Δ*z* refer to a setpoint of $V = 0.2$ V, $I = 1.0$ pA in (**a-f**) and of $V = 0.2$ V, $I = 0.5$ pA in (**g–i**). All scale bars 5 Å.

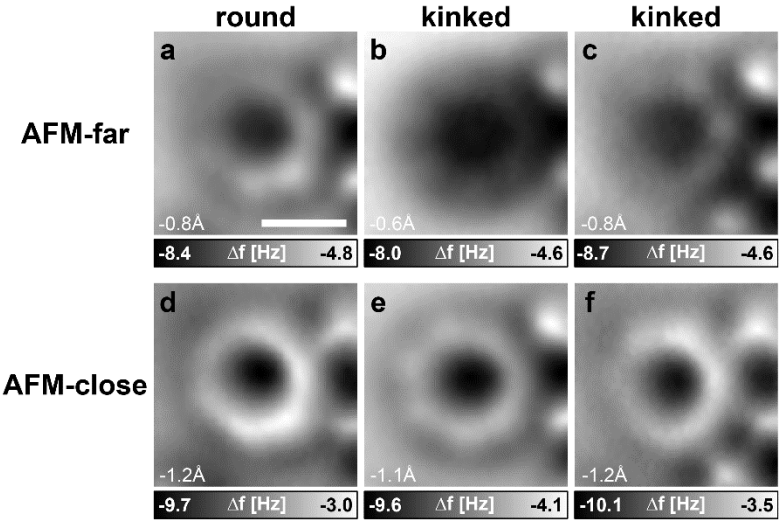

Figure S14. Raw AFM data of Fig. 2. Laplace-filtered images of this AFM data are shown in Fig. 2, A to F of the main text. (a–c) AFM-far, (d–f) AFM-close, with respective tip-height offset Δ*z* indicated. Scale bar 5 Å, applies to all images.

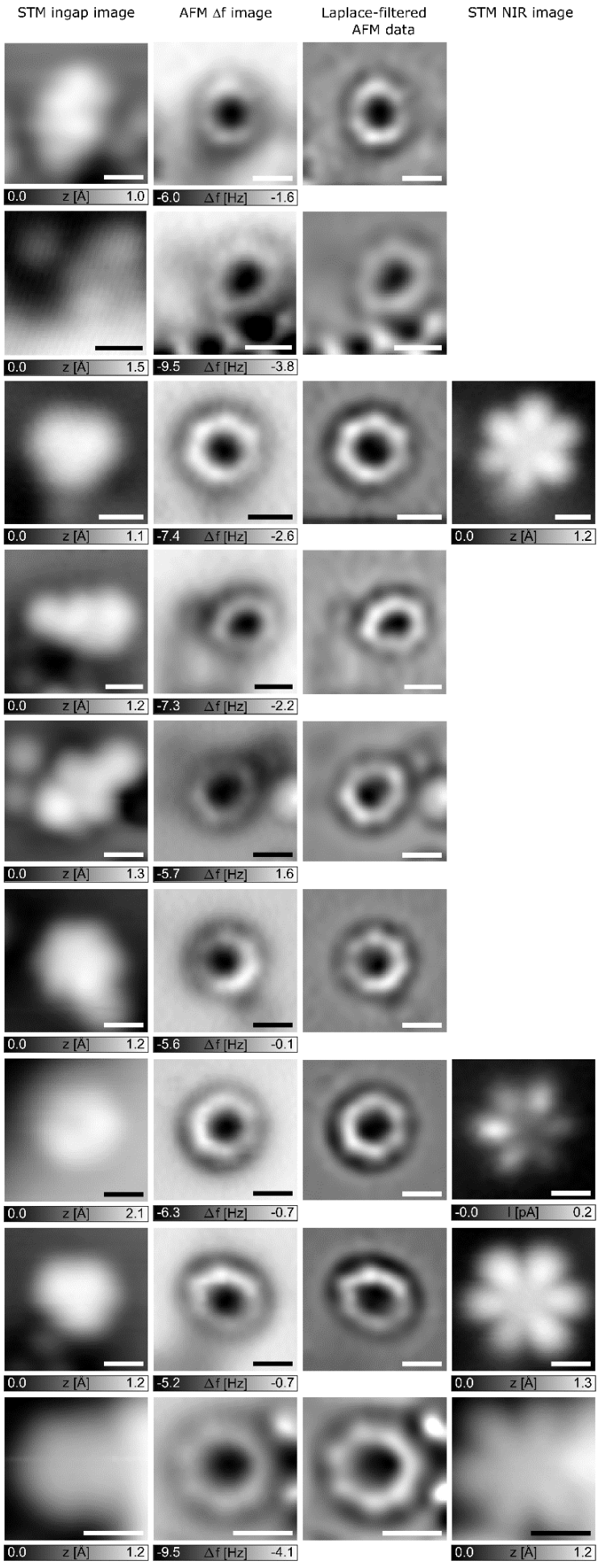

Figure S15. Additional AFM and STM data on different C_{13} molecules.
Experimental data of nine different individual C_{13} molecules. Each row shows the same individual molecule. The first column shows in-gap STM images (V = 0.2 V), the second column raw AFM data, the third column the respective Laplace-filtered AFM data. For the molecules that were adsorbed stably enough to obtain STM data at the NIR, the fourth column shows a STM image at V = 1 V. The NIR image in the third from bottom row was recorded in constant-height mode, all other STM images (including those shown in the main text) were acquired in constant-current mode. Scale bars 5 Å.

6. Computational details

Optimization. CASPT2 geometry optimizations of C_{13} were done in two steps. First, a rough optimization was performed with the default *SLAPAF* settings until the energy started oscillating. In the second step, the keywords *C2-DIIS*, *CARTESIAN*, and a smaller *MAXSTEP* (between 0.1 and 0.05, depending on the system) were added. This reduced the energy by an additional ~10 mHa relative to the first optimization, and usually resulted in an energy converging to within ~0.2 mHa. Point charges for the surface calculations, which included two layers (290 point-charges), were added via the *XFIELD* keyword.
The first CASSCF/CASPT2 triplet of C_{13} was always $^3|21\ 21\rangle$. In a single-state singlet calculation, the first CASSCF/CASPT2 root was either $^1|22\ 20\rangle$ (when the kink was large in the gas phase and at a positive adatom on surface) or $^1|20\ 22\rangle$ (when the kink was small in the gas phase and on the pristine surface, and at a negative adatom on surface). In a two-state calculation the second CASSCF root (but lower in CASPT2 energy) was always $^1|21\ 21\rangle$, optimizing to a geometry very similar to $^3|21\ 21\rangle$ in all investigated environments. In the presence of point charges (on the surface), the optimized geometries of all three roots were very similar, with κ differing by about 1°.

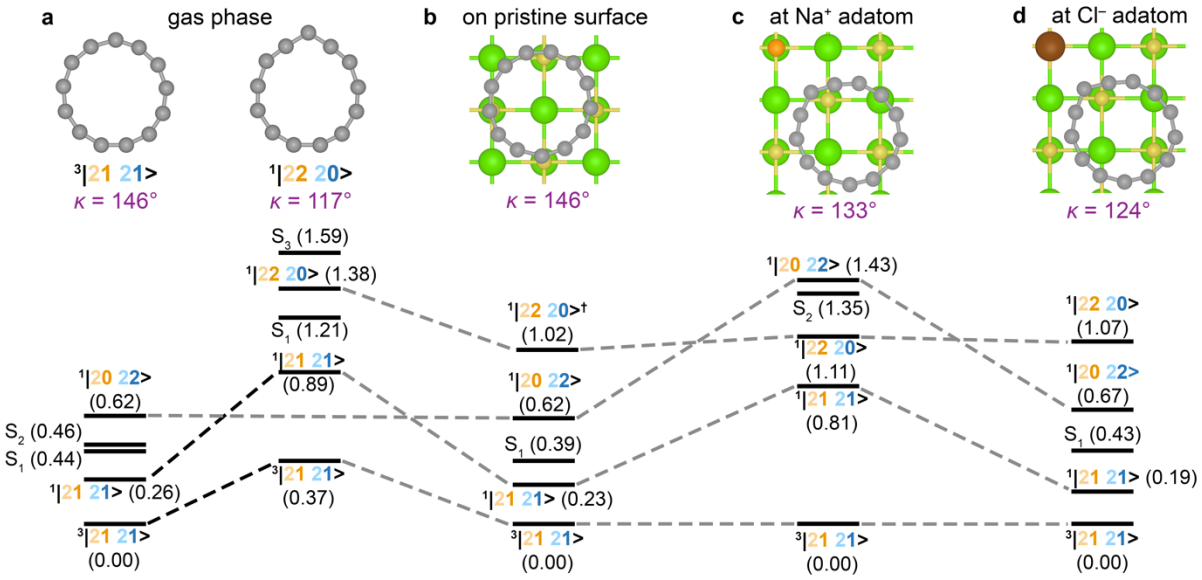

Figure S16. Electronic states and energies (in eV) of C_{13} calculated using multistate CASPT2. **a**, gas phase results at the optimized $^3|21\ 21\rangle$ triplet and $^1|22\ 20\rangle$ singlet geometry. **b–d**, on-surface results at the pristine surface (b) and at the positive (c) and negative (d) adatom, calculated at the optimized triplet geometry. Black lines connect states with similar composition in the same environment, and gray lines across different environments. †The $^1|22\ 20\rangle$ state in (b) was not found at the optimized triplet geometry; the result shown is for the $^1|20\ 22\rangle$ singlet optimized geometry with κ = 145°.

Single point CASPT2 energies. The combination of a triple-zeta basis set, large active space (14,12), and a multistate calculation with four roots resulted in significant multireference character of all states. Energies of calculated states are compared in fig. S16. Shown at the triplet geometry (left hand side) and the |22 20> geometry (right-hand side) in fig. S16a, with

approximate assignments of selected states. We note that the compositions of excited states are strongly dependent on the number of requested roots and the mixing scheme, i.e., state-averaged vs. multistate vs. extended multistate CASPT2, suggesting strong mixing between the states. A curiosity, which we noticed is that mixing the two closed-shell singlets, i.e., $\psi \approx {}^1|22\ 20\rangle + {}^1|20\ 22\rangle$, leads to a twisted Hückel topology (*48*).

Dyson orbitals were calculated from the self-consistent CASPT2 wavefunctions, using the *RASSI* module in OpenMolcas. In all cases, the Dyson norms were 0.85–0.92, indicating that little orbital relaxation occurs upon electron attachment, i.e. that $\psi^{n+1} \approx \psi^{n}\ \psi^{LUMO}$.

Effect of the kink. As indicated in Fig. 3, B and C, the kink affects the relative energies of the B′ and B″ orbitals. This is reflected in the ordering of the electron affinities for electron insertion into the out-of-plane π-system, which results in the ${}^2|21\ 22\rangle$ state, and into the in-plane π-system, leading to ${}^2|22\ 21\rangle$. However, as the energetic separation between them is small, the ordering of B′ and B″ orbitals has no considerable effect on the triplet ${}^3|21\ 21\rangle$ ground state.
In the gas phase, when the kink is small ($\kappa \geq 133°$) the ${}^2|21\ 22\rangle$ state (corresponding to electron attachment into the out-of-plane π-system) is lower in energy than ${}^2|22\ 21\rangle$. As the distortion gets bigger ($\kappa < 133°$), the order reverses and the ${}^2|22\ 21\rangle$ state (corresponding to electron attachment into the in-plane π-system) becomes lower in energy (fig. S17).

Increasing the kink localizes the spin density (fig. S18), also localizes the density for both in-plane and out-of-plane Dyson orbitals at the kink position (fig. S17). In correspondence, in the experiment, a lobe with increased density is observed above the kink for the "kinked" C_{13} (see Fig. 2, H and I).
In the optimized geometry on a pristine surface ($\kappa = 148°$, Fig. 3, E and I) and at a positively charged adatom ($\kappa = 133°$, Fig. 3, F and J) the electron affinity is lower (more negative) for inserting the electron in the out-of-plane π-system. Moreover, the Dyson orbital's density is more localized on the kink in the latter case. In the optimized geometry at a negatively charged adatom ($\kappa = 124°$, Fig. 3, G and K) inserting an electron in the in-plane system is energetically more favorable. At a negatively charged adatom, the density is not very localized at the kink due to Columbic repulsion, approximately compensating the effect of density localization due to the kink.

For the interpretation of the STM maps of the NIR of C_{13} (Fig. 2, G to I) it is important to consider that the tip, which is positioned above the ring, has a larger overlap of its wavefunctions with the out-of-plane system than with the in-plane system. Therefore, if transitions to both systems are possible (if their energy difference is smaller than, or similar to the peak broadening, which is 0.3 eV on NaCl (*32*)), tunneling into the out-of-plane system is expected to be the dominant channel for electron attachment. This explains why the NIR maps are expected to be dominated by out-of-plane Dyson orbitals, even if the in-plane orbital is slightly closer to the Fermi level, see Fig. 3K and L, and fig. S12. The same argument explains why the PIR of C_{26} (Fig. 4L) appears in the shape of out-of-plane orbital densities (Fig. 4H).

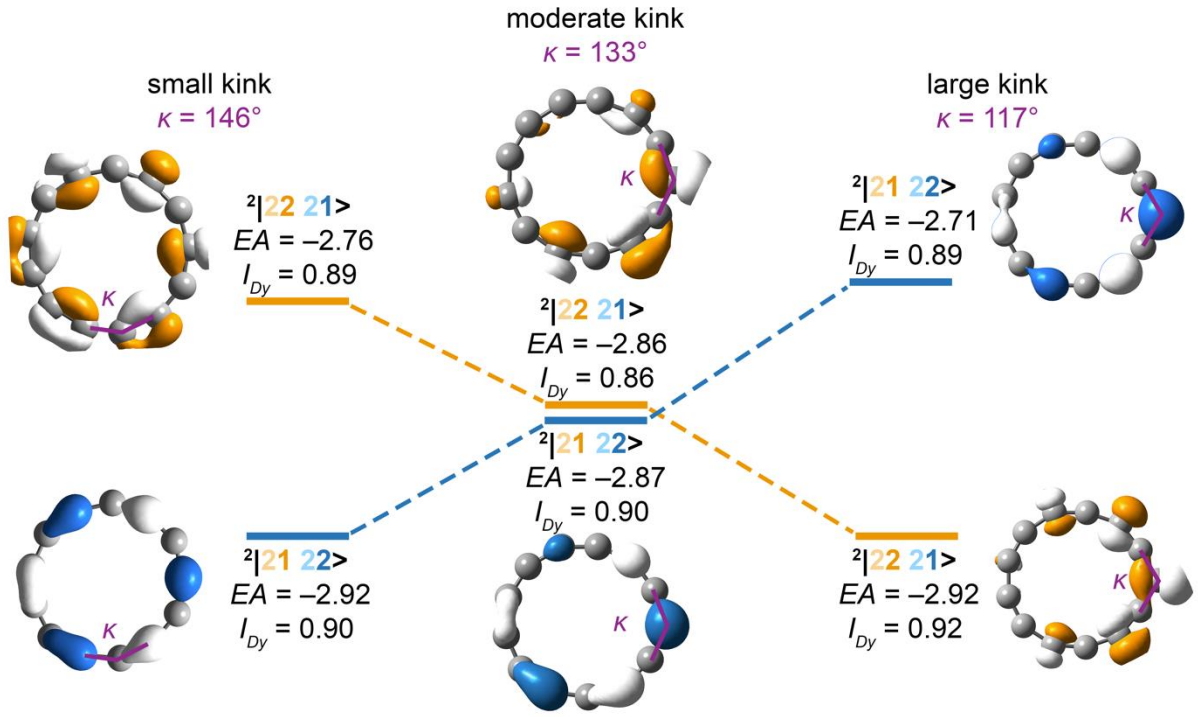

Figure S17. Dyson orbitals (at 0.05 a.u.) for electron attachment, their intensities (I_{Dy}) and electron affinities (*EA*) at three different kink values, calculated using CASPT2(12,14) in the gas phase.

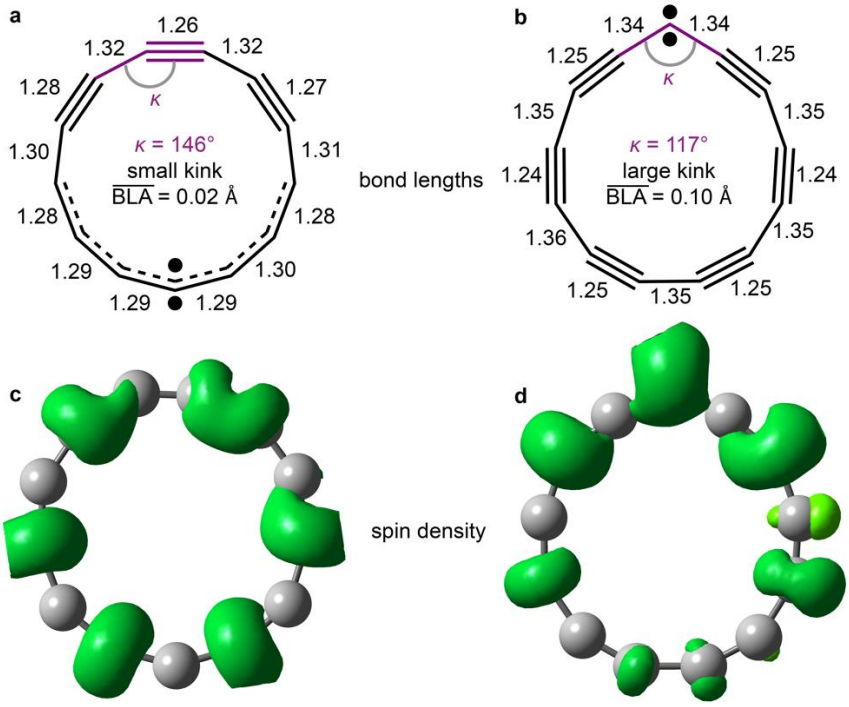

Figure S18. (**a**, **b**) Bond lengths in Å. (**c**, **d**) Spin densities of C_{13} in the ground triplet state at small (a, c) and large (b, d) kink values, calculated using CASPT2(12,14) in the gas phase. Spin density (green) at 0.005 a.u.

Quantum simulations. Following previous work of some of the authors (*2*, *14*), we also employed quantum-computing. Here, we calculated Dyson orbitals using a quantum-computing algorithm. Specifically, we optimized the electronic wave function of C_{13} with the variational quantum eigensolver (VQE) based on the unitary coupled cluster with single and double excitations (qUCCSD) ansatz. All simulations were carried out with the statevector simulator as implemented in the Qiskit package. All qUCCSD calculations are based on the cc-pVTZ basis set, on an active space comprising 4 orbitals and 6 electrons, and on molecular orbitals optimized with the state-average complete active space self-consistent field algorithm as implemented in OpenMolcas (*49*) by averaging the electronic energy over the 5 lowest-energy states. In all cases, we included in the qUCCSD ansatz only excitation operators preserving the spin S_z operator (simulations including also spin-flip excitation operators yield the same qualitative trend discussed below).

qUCCSD predicts the ground state to be the closed-shell singlet $^1|22\ 20>$. This does not agree with the CASPT2 results, but matches the trend observed using CASSCF (*13*). This is to be expected since, as CASSCF, also qUCCSD neglects dynamical correlation effects, which are included in CASPT2. Nevertheless, as we show in fig. S19, qUCCSD correctly predicts the shape and relative energy ordering of the two lowest electron-affinity Dyson orbitals. The latter were obtained based on the lowest-energy triplet wave function, obtained by applying optimizing with VQE a qUCCSD ansatz constructed starting from a determinant composed of 4 alpha and 2 beta electrons, and the two lowest-energy anionic state, optimized with the variational quantum deflation algorithm (*50*). We calculated the Dyson orbitals by converting the optimized qUCCSD wave functions to their statevector representation and, subsequently, applying the algorithm described in (*51*) for calculating Dyson orbitals based on configuration interaction-type wave functions. As we report in fig. S19, qUCCSD correctly predicts the relative energetic ordering of the Dyson orbitals both for the small-kink and for the large-kink geometries. In agreement with the CASPT2 results, the lowest electron affinity Dyson orbital is out-of-plane for the small kink value, and in-plane for the large kink value. This indicates that dynamical correlation does not play a crucial role in predicting the qualitative shape of the Dyson orbitals. The latter can, therefore, be efficiently predicted with quantum-computing simulations, which can efficiently capture strong, static correlation effects.

We note that, although in this work we used classical simulators of the quantum-computing calculation, it would be possible to calculate the Dyson orbitals directly on quantum hardware based on the algorithm described in (*14*). Moreover, we note that this is, up to our knowledge, the first proposal for a quantum computing-based calculation of Dyson orbitals.

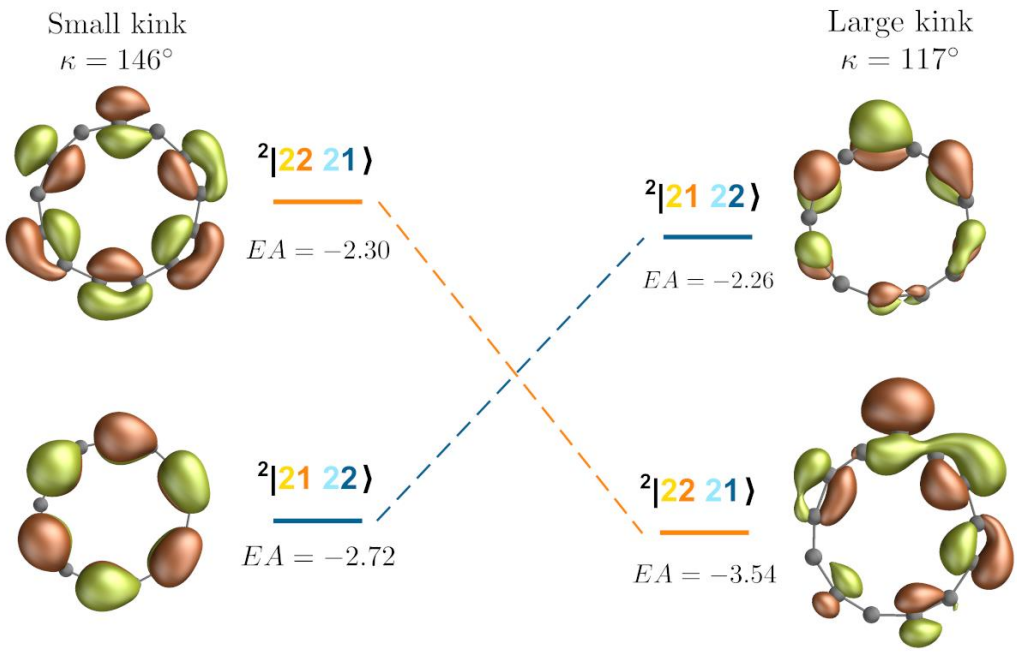

Figure S19. Dyson orbitals (at 0.05 a.u.) and corresponding electron affinities (*EA*) for electron attachment calculated with qUCCSD based on the cc-pVTZ basis set and an active space including 6 electrons and 4 orbitals. Dyson orbitals were calculated both for the "small kink" geometry, corresponding to the triplet equilibrium geometry (left part of the figure), and for the "large kink" geometry, corresponding to the closed-shell singlet equilibrium geometry (right part of the figure). Electron affinities (*EA*) in eV.

Explicitly correlated coupled clusters with singles, doubles and perturbative iterative triples (*52*) were done using the domain based local pair-natural orbital framework, F12-DLPNO-CCSD(T*). The calculations utilized the explicitly correlated cc-pVDZ-F12 basis, which gives results comparable to a 2-3 tier larger noncorrelated basis (*53, 54*). Single-point energies for two gas-phase geometries of C_{13} in the lowest singlet and triplet state are shown in fig. S20, but we note that the large values of the T_1 diagnostic make these results somewhat unreliable. These calculations were done using ORCA (*55*).

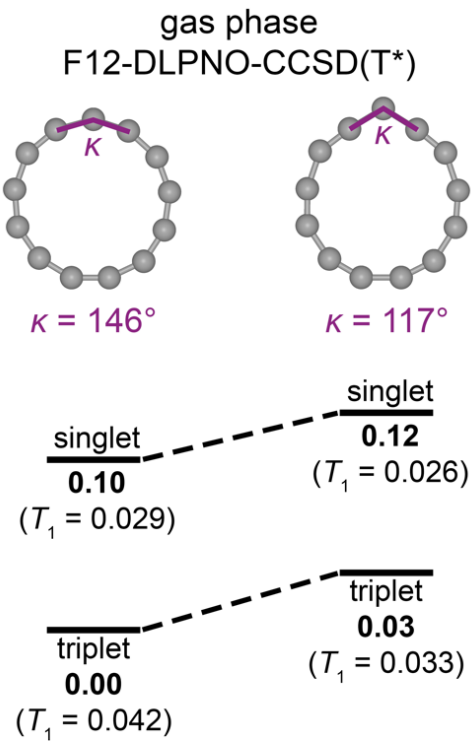

Figure S20. Relative energies (bold, in eV) of C_{13} in its singlet and triplet ground state, calculated using F12-DPLNO-CCSD(T*)/F12-cc-pVDZ at gas phase optimized geometries. The T_1 diagnostic values, which give a measure of multireference nature, are given in parentheses.

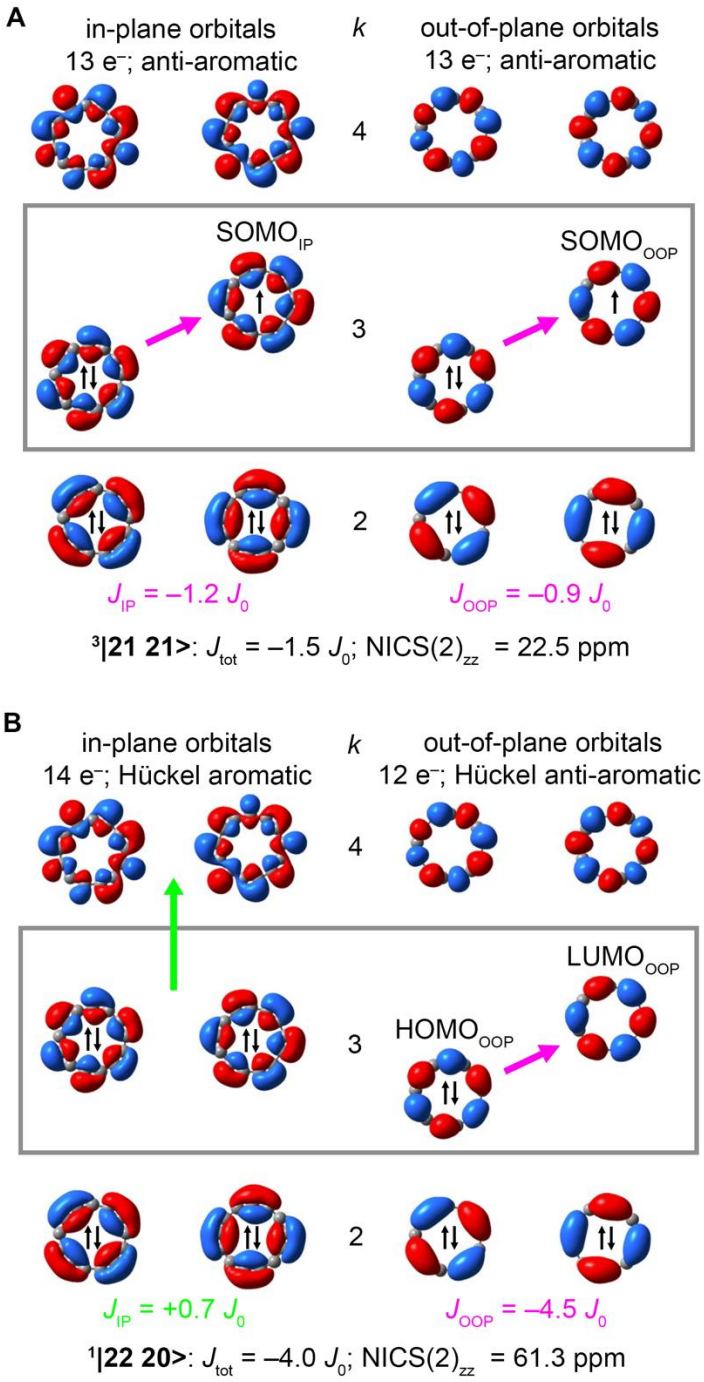

Figure S21. Aromaticity and molecular orbitals of C_{13} in CASPT2-optimized gas phase geometries in (**A**) the $^3|21\ 21>$ state and (**B**) the $^1|22\ 20>$ state, calculated using ωB97XD/def2-TZVP. In-plane (left column) and out-of-plane (right column) orbitals with angular momentum k = 2–4. The four frontier orbitals with k = *3* are highlighted with gray rectangles. The arrows show the major aromatic (green) and anti-aromatic (purple) transitions in each π-system along with their respective contributions (labelled as J_{IP} and J_{OOP}), as calculated using SYSMOIC (*56*). The z-component of nucleus independent chemical shift (NICS) values calculated 2 Å above the center of the molecule are also shown. We also note that transitions in the $^3|21\ 21>$ state of C_{13} resemble the S_1 state of C_{16} (both π-systems odd-numbered) while $^1|2220>$ resembles T_1 of C_{16} (one π-system aromatic, the other anti-aromatic), see ref (*14*).

7. Additional experimental data on C_{26}

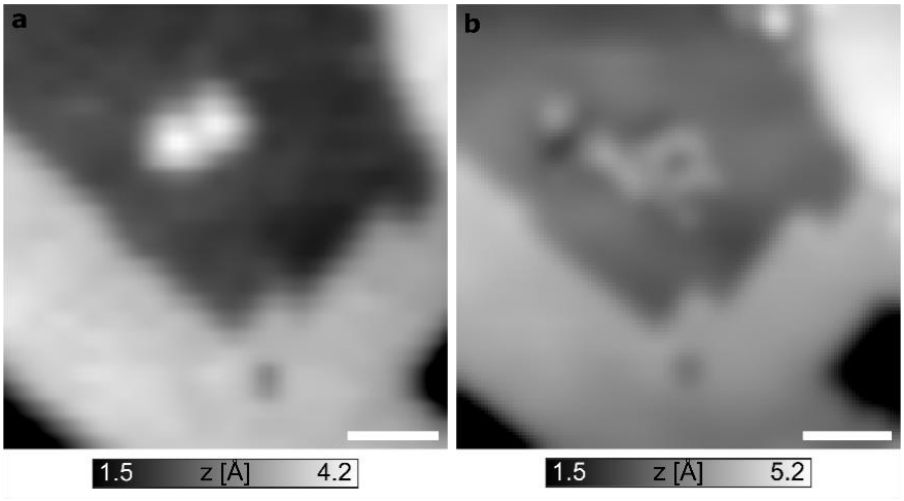

Figure S22. **Cyclo[26]carbon generation.** STM images (V = 0.1 V, I = 0.5 pA) of (**a**) two adjacently adsorbed precursor molecules and (**b**) same sample area after applying a voltage pulse of V = 4.3 V, in this case at a constant current of I = 1.0 pA, resulting in the formation of cyclo[26]carbon, C_{26} (**b**). (**a**) recorded with a metallic tip, (**b**) recorded with a CO-functionalized tip. AFM data and STM orbital density maps of the C_{26} molecule imaged in (b) are shown in the main text in Fig. 4. Scale bars 20 Å.

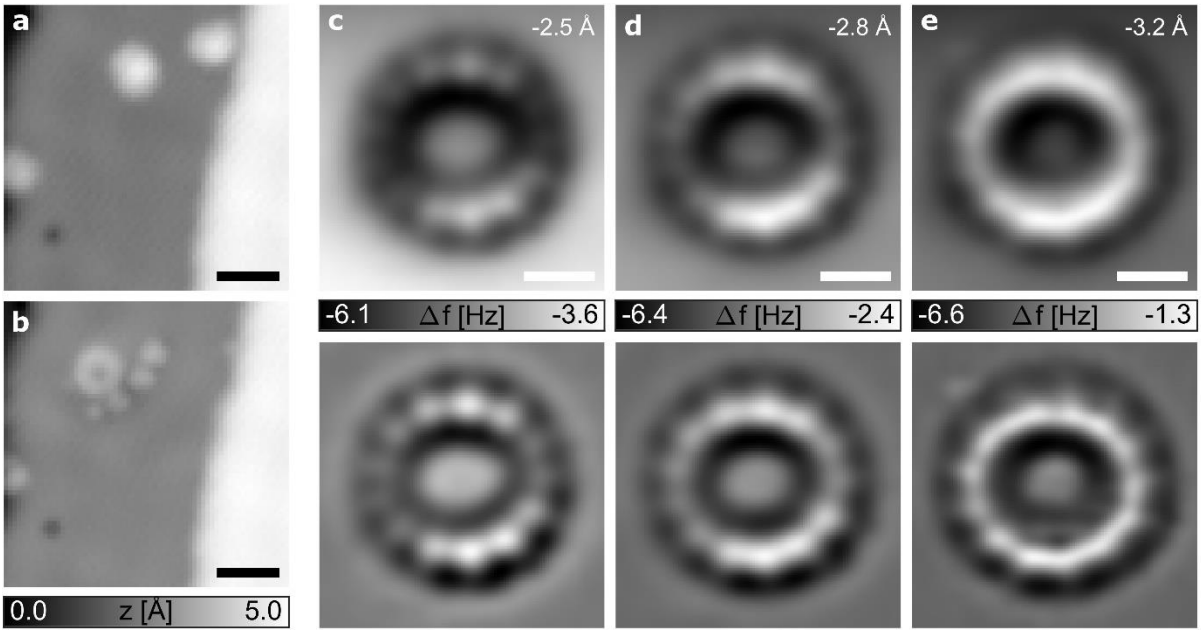

Figure S23. **Additional (high-resolution AFM) data on Cyclo[26]carbon.** STM images (V = 0.2 V, I = 0.3 pA) before (**a**) and after (**b**) applying a voltage pulse of V = 4.4 V to form the cyclo[26]carbon shown in this figure, from two adjacently adsorbed precursor molecules. (**c-e**) AFM images recorded at Δz indicated in each panel with respect to a setpoint of I = 0.3 pA and V = 0.2 V; lower panels show Laplace-filtered data. Scale bars 20 Å in (a, b), 5 Å in (c-e).

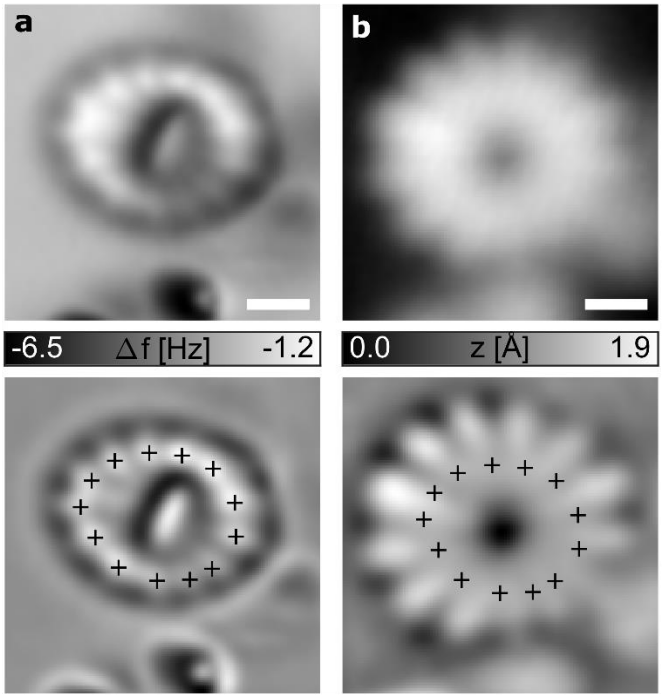

Figure S24. Additional (AFM and STM) data on Cyclo[26]carbon. (**a**) AFM (Δz = -1.5 Å with respect to a setpoint of I = 0.3 pA and V = 0.2 V). (**b**) STM data at the NIR (V = 1.5 V, I = 0.3 pA). The lower panels show Laplace filtered data. As for the cyclo[26]carbon shown in Fig. 4 of the main text, the 13 lobes of high density of the NIR are located above the long bonds of C_{26}, i.e., between the marks assigning the short bonds by the corresponding AFM image. We relate the asymmetry in the AFM image (a) to an asymmetric CO tip. The molecule is the same C_{26} as imaged in fig. S23, imaged with a different tip and at a different adsorption site. Scale bars 5 Å.

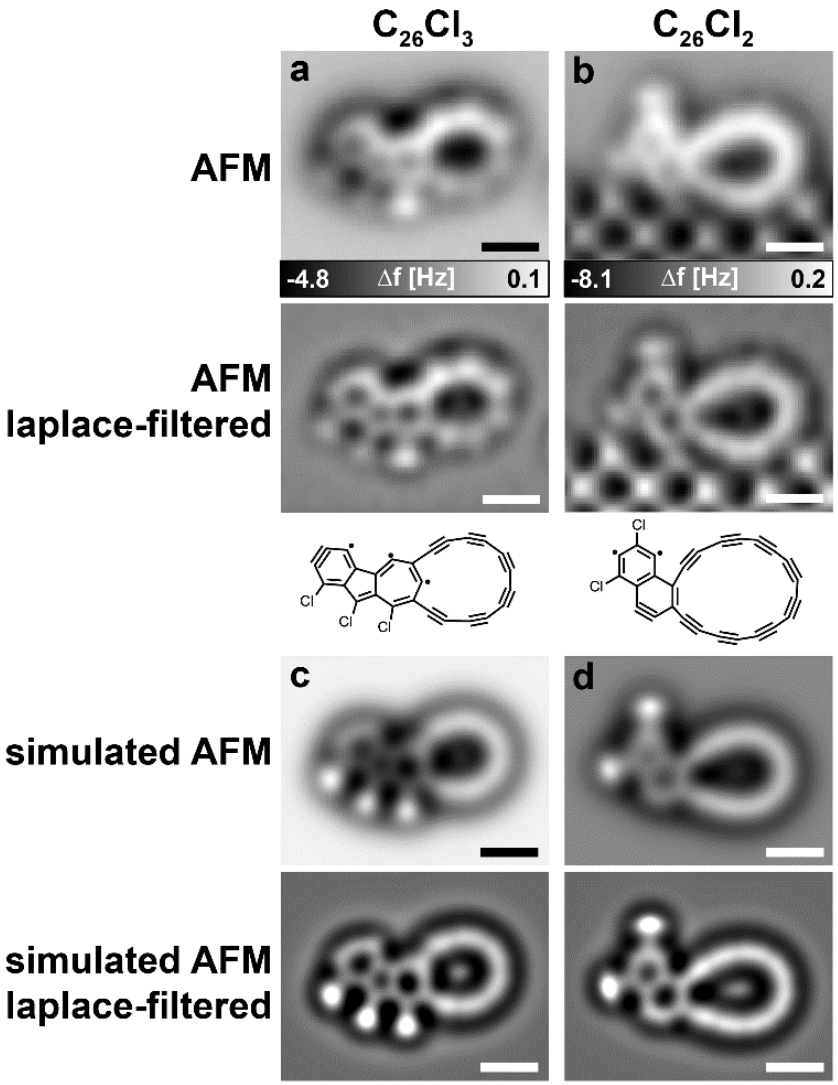

Figure S25. **Partly dehalogenated dimers generated by on-surface synthesis.** (**a, b**) AFM data (top), corresponding Laplace-filtered data (middle) and tentatively assigned Kekule structures (bottom). After a first voltage pulse of V = 4.5 V above two precursor molecules in close proximity on bilayer NaCl, the molecule in (a) was observed on bilayer NaCl. Applying another voltage pulse above the molecule in (a) resulted in the molecule shown in (b) and a change of its adsorption site. The molecule moved to monolayer NaCl where it is adsorbed next to a bilayer NaCl step edge, that is imaged in the bottom part of (b). (**c, d**) Simulated AFM images of proposed structures and corresponding Laplace-filtered images. Simulations of AFM images were performed based on DFT calculated xyz geometries using the Probe-Particle Model (*28*) using default CO-tip parameters (stiffness $k_x = k_y$ = 0.25 N/m, k_R = 30 N/m), at an oscillation amplitude of A = 0.5 Å and a tip distance from the highest atom of 6.8 Å (c) and 6.7 Å (d). Scale bars 5 Å.